The Astrophysical Journal Supplement Series, 257:6 (18pp), 2021 November https://doi.org/10.3847/1538-4365/ac1440

Molecules with ALMA at Planet-forming Scales (MAPS). VI. Distribution of the Small Organics HCN, C_2H, and H_2CO

Viviana V. Guzmán[1], Jennifer B. Bergner[2,22], Charles J. Law[3], Karin I. Öberg[3], Catherine Walsh[4], Gianni Cataldi[5,6], Yuri Aikawa[6], Edwin A. Bergin[7], Ian Czekala[8,9,10,11,12,22], Jane Huang[3,7,22], Sean M. Andrews[3], Ryan A. Loomis[13], Ke Zhang[7,14,23], Romane Le Gal[3,15,16,17], Felipe Alarcón[7], John D. Ilee[4], Richard Teague[3], L. Ilsedore Cleeves[18], David J. Wilner[3], Feng Long[3], Kamber R. Schwarz[19,22], Arthur D. Bosman[7], Laura M. Pérez[20], François Ménard[16], and Yao Liu[21]

[1] Instituto de Astrofísica, Pontificia Universidad Católica de Chile, Av. Vicuña Mackenna 4860, 7820436 Macul, Santiago, Chile; vguzman@astro.puc.cl
[2] University of Chicago, Department of the Geophysical Sciences, Chicago, IL 60637, USA
[3] Center for Astrophysics | Harvard & Smithsonian, 60 Garden St., Cambridge, MA 02138, USA
[4] School of Physics and Astronomy, University of Leeds, Leeds, LS2 9JT, UK
[5] National Astronomical Observatory of Japan, 2-21-1 Osawa, Mitaka, Tokyo 181-8588, Japan
[6] Department of Astronomy, Graduate School of Science, The University of Tokyo, Tokyo 113-0033, Japan
[7] Department of Astronomy, University of Michigan, 323 West Hall, 1085 S. University Avenue, Ann Arbor, MI 48109, USA
[8] Department of Astronomy and Astrophysics, 525 Davey Laboratory, The Pennsylvania State University, University Park, PA 16802, USA
[9] Center for Exoplanets and Habitable Worlds, 525 Davey Laboratory, The Pennsylvania State University, University Park, PA 16802, USA
[10] Center for Astrostatistics, 525 Davey Laboratory, The Pennsylvania State University, University Park, PA 16802, USA
[11] Institute for Computational & Data Sciences, The Pennsylvania State University, University Park, PA 16802, USA
[12] Department of Astronomy, 501 Campbell Hall, University of California, Berkeley, CA 94720-3411, USA
[13] National Radio Astronomy Observatory, 520 Edgemont Rd., Charlottesville, VA 22903, USA
[14] Department of Astronomy, University of Wisconsin-Madison, 475 N. Charter St, Madison, WI 53706, USA
[15] IRAP, Université de Toulouse, CNRS, CNES, UT3, Toulouse, France
[16] Univ. Grenoble Alpes, CNRS, IPAG, F-38000 Grenoble, France
[17] IRAM, 300 rue de la piscine, F-38406 Saint-Martin d'Hères, France
[18] Department of Astronomy, University of Virginia, Charlottesville, VA 22904, USA
[19] Lunar and Planetary Laboratory, University of Arizona, 1629 E. University Blvd, Tucson, AZ 85721, USA
[20] Departamento de Astronomía, Universidad de Chile, Camino El Observatorio 1515, Las Condes, Santiago, Chile
[21] Purple Mountain Observatory & Key Laboratory for Radio Astronomy, Chinese Academy of Sciences, Nanjing 210023, People's Republic of China
Received 2021 March 1; revised 2021 July 13; accepted 2021 July 14; published 2021 November 3

Abstract

Small organic molecules, such as C_2H, HCN, and H_2CO, are tracers of the C, N, and O budget in protoplanetary disks. We present high-angular-resolution (10–50 au) observations of C_2H, HCN, and H_2CO lines in five protoplanetary disks from the Molecules with ALMA at Planet-forming Scales (MAPS) ALMA Large Program. We derive column density and excitation temperature profiles for HCN and C_2H, and find that the HCN emission arises in a temperate (20–30 K) layer in the disk, while C_2H is present in relatively warmer (20–60 K) layers. In the case of HD 163296, we find a decrease in column density for HCN and C_2H inside one of the dust gaps near ∼83 au, where a planet has been proposed to be located. We derive H_2CO column density profiles assuming temperatures between 20 and 50 K, and find slightly higher column densities in the colder disks around T Tauri stars than around Herbig Ae stars. The H_2CO column densities rise near the location of the CO snowline and/or millimeter dust edge, suggesting an efficient release of H_2CO ices in the outer disk. Finally, we find that the inner 50 au of these disks are rich in organic species, with abundances relative to water that are similar to cometary values. Comets could therefore deliver water and key organics to future planets in these disks, similar to what might have happened here on Earth. This paper is part of the MAPS special issue of the Astrophysical Journal Supplement.

Unified Astronomy Thesaurus concepts: Protoplanetary disks (1300)

1. Introduction

Young stars have flattened disks of gas and dust rotating around them, a natural outcome of the star formation process. The material available in these protoplanetary disks will eventually be accreted onto the star, blown out by winds, or be incorporated into planets (see reviews by Williams & Cieza 2011; Andrews 2020; Öberg & Bergin 2021). The chemical composition of nascent planets is therefore directly linked to the chemical reservoir of disks. Small organics are some of the main carriers of C, N, and O in protoplanetary disks. However, the ability of planets to access these organic reservoirs depends on the distribution of this material, particularly in the inner few tens of astronomical units where rocky planets are expected to form.

Although the main carrier of N in disks is expected to be N_2, this molecule has no observable lines in cold gas. HCN is a secondary N carrier, but its rotational lines in the millimeter are readily detected in disks (Öberg et al. 2011; Chapillon et al. 2012; Bergner et al. 2019). In addition, observations of mid-infrared HCN lines have shown that it is abundant in the inner ∼10 au of disks (Salyk et al. 2011; Najita et al. 2013, 2018).

[22] NASA Hubble Fellowship Program Sagan Fellow.
[23] NASA Hubble Fellow.

HCN is therefore one of our best tracers of the N budget in disks and allows us to characterize the spatial distribution of N. Moreover, HCN is thought to be a crucial molecule to the emergence of life, as it is the starting point in the chemistry leading to proteins and RNA (Powner et al. 2009; Patel et al. 2015; Becker et al. 2019).

In addition to revealing the distribution of the organic and elemental reservoir, molecular lines provide us key information on the physical and chemical conditions prevailing in disks. The distribution of HCN and C_2H has been shown to depend on the UV radiation field and on the abundances of C and O (Du et al. 2015; Bergin et al. 2016; Cleeves et al. 2018). The distribution of these small organics are also potentially sensitive to density and temperature variations. For example, HCN has been proposed to be a useful tool to study the formation of giant planets in disks, as they will heat up the surrounding gas and result in enhanced HCN emission around the forming planet (Cleeves et al. 2015).

H_2CO is a third commonly observed small organic in disks that is connected to the oxygen cycle. It is an important precursor of O-bearing Complex Organic Molecules (COMs), such as methanol, acetaldehyde, ethylene glycol, and formamide (Watanabe & Kouchi 2002; Chuang et al. 2017). It is hypothesised that O-bearing COMs are preferentially locked in ices and removed from the gas phase as the dust grows and settles to the midplane (e.g., Bergin et al. 2010; Hogerheijde et al. 2011; Du et al. 2017). This would explain why O-bearing COMs have been more difficult to detect in disks compared to nitriles or hydrocarbons (e.g., Chapillon et al. 2012; Öberg et al. 2015; Walsh et al. 2016; Bergner et al. 2018; Favre et al. 2018; Loomis et al. 2018; Carney et al. 2019). H_2CO lines, however, are much brighter in disks than lines from more complex O-bearing species because H_2CO has a simpler molecular structure and therefore the internal energy is distributed in fewer molecular lines (Aikawa et al. 2003; Pegues et al. 2020). Observations of H_2CO therefore provide a view of the spatial distribution of the O-bearing molecules in disks.

While rich substructure has been observed in dust continuum emission of numerous disks (e.g., Andrews et al. 2018; Long et al. 2018; Pérez et al. 2020), the chemical structure of these disks has been less explored at high angular resolution. The combination of sensitivity and spatial resolution needed to spatially resolve molecular line emission on planet-forming scales has been the main limitation so far in characterizing the distribution of most key organic molecules. However, sensitive observations at moderate angular resolution have demonstrated the presence of a rich substructure in the emission of various molecular lines (e.g., Henning & Semenov 2008; Mathews et al. 2013; Öberg et al. 2015; Bergin et al. 2016; Huang et al. 2017; Öberg et al. 2017; Salinas et al. 2017; Cazzoletti et al. 2018; Kastner et al. 2018; Miotello et al. 2019; Pegues et al. 2020; Teague & Loomis 2020).

In this paper, we present observations from the Molecules with ALMA at Planet-forming Scales (MAPS) ALMA Large Program. Here, we focus on molecular line emission from the small organic molecules HCN, C_2H, and H_2CO in five nearby and otherwise well-studied protoplanetary disks. HCN, C_2H, and H_2CO have been previously observed in these disks, but at lower angular resolution ($\sim 0\farcs5$). In particular, Bergner et al. (2019) presented observations of HCN and C_2H toward four of these disks, and Pegues et al. (2020) presented observations of H_2CO toward the five disks. The MAPS data presented in this paper provide a combination of high angular resolution with excellent brightness sensitivity, which enables us to identify substructure in the line emission of these small organics. The observations are briefly described in Section 2. In Section 3, we present the spatial distribution of the emission. In Section 4, we retrieve the column density and excitation temperature profiles. We discuss the results in Section 5, and summarize our conclusions in Section 6.

Table 1
Source Characterization of the MAPS Sample

Source	Spectral Type	Distance (pc)	Incl (deg)	PA (deg)	$M_\star$ ($M_\odot$)
IM Lup	K5	158	47.5	144.5	1.1
GM Aur	K6	159	53.2	57.2	1.1
AS 209	K5	121	35.0	85.8	1.2
HD 162396	A1	101	46.7	133.3	2.0
MWC 480	A5	162	37.0	148.0	2.1

Note. Reproduced from Öberg et al. (2021), where additional source characteristics and a list of references are provided.

2. Observations

The observations are part of the MAPS ALMA Large Program (2018.1.01055.L), where a large number of molecular lines were observed at high spatial resolution to search for links between chemistry and planet formation in protoplanetary disks. See Öberg et al. (2021) for a detailed description of the scope and aims of MAPS. The MAPS sample includes disks around both T Tauri (IM Lup, GM Aur, and AS 209) and Herbig Ae (HD 163296 and MWC 480) stars, with a wide variety of dust substructures (e.g., rings, gaps, and spirals). A detailed description of the sources can be found in Öberg et al. (2021), and a brief summary is given in Table 1.

Four spectral settings, two in Band 6 and two in Band 3, were observed between 2019 and 2020. The Band 6 setting covered the HCN $J = 3$–2, C_2H $N = 3 - 2$, and the H_2CO $3_{03} - 2_{02}$ lines. The Band 3 setting covered the HCN $J = 1$–0 lines and the C_2H $N = 1$–0 ladder. See Table 2 for a full list of QNs or transitions observed. We subsequently just refer to these lines as 3–2 and 1–0, for simplicity. The data include observations using two different array configurations, to provide sufficient dynamic range in baseline length to recover both large-scale and small-scale emission.

The data were first calibrated by the ALMA staff using standard routines, and then self-calibrated by the MAPS team to improve the signal-to-noise ratio (S/N) of the data. A detailed description of the observations and calibration process can be found in Öberg et al. (2021).

The imaging of the observed visibilities was done with the `tclean` task of the `CASA` 6 software. A Keplerian mask was created during the CLEANing process, by selecting regions in each channel where line emission is expected given the Keplerian rotation of each disk. Novel techniques were applied to improve the image quality, in particular the scaling of the CLEAN residual map, which can affect substantially the data quality when combining data from different configuration arrays. We encourage the reader to read a more detailed description of the imaging strategy in Czekala et al. (2021).

We make use of the fiducial MAPS images, which have a circular beam of $0\farcs15$ (corresponding to linear spatial scales of 15–24 au) for the 3–2 lines, and a circular beam of $0\farcs3$

Table 2
Spectroscopic Constants of the Observed Lines

Molecule	Transition	ν (GHz)	$S_{ij}\mu^2$ (D^2)	$\log_{10}(A_{ij})$ (s^{-1})	E_u (K)	g_u	v_i[a] (km s^{-1})	r_i[b]
HCN	$J = 1–0$, $F = 1–1$	88.630415	8.91247	−4.61844	4.2	3	4.8	0.600
	$J = 1–0$, $F = 2–1$	88.631847	14.85197	−4.61848	4.2	5	0.0	1.000
	$J = 1–0$, $F = 0–1$	88.633935	2.97073	−4.61840	4.2	1	−7.1	0.200
	$J = 3–2$, $F = 3–3$	265.884891	2.97015	−4.03231	25.5	7	1.8	0.086
	$J = 3–2$, $F = 2–1$	265.886188	16.03887	−3.15378	25.5	5	0.4	0.467
	$J = 3–2$, $F = 3–2$	265.886433	23.76144	−3.12920	25.5	7	0.1	0.691
	$J = 3–2$, $F = 4–3$	265.886499	34.36945	−3.07805	25.5	9	0.0	1.000
	$J = 3–2$, $F = 2–3$	265.886979	0.08487	−5.43017	25.5	5	−0.5	0.002
	$J = 3–2$, $F = 2–2$	265.888522	2.97075	−3.88607	25.5	5	−2.3	0.086
C_2H	$N = 1–0$, $J = 3/2$-$1/2$, $F = 2–1$	87.316925	1.42458	−5.65605	4.2	5	0.0	1.000
	$N = 1–0$, $J = 3/2$-$1/2$, $F = 1–0$	87.328624	0.70952	−5.73675	4.2	3	−40.2	0.498
	$N = 3–2$, $J = 7/2–5/2$, $F = 4–3$	262.004226	3.29692	−4.11528	25.1	9	0.0	1.000
	$N = 3–2$, $J = 7/2–5/2$, $F = 3–2$	262.006403	2.46660	−4.13213	25.1	7	−2.5	0.748
	$N = 3–2$, $J = 5/2$-$3/2$, $F = 3–2$	262.064843	2.35407	−4.15212	25.2	7	−69.4	0.714
	$N = 3–2$, $J = 5/2$-$3/2$, $F = 2–1$	262.067331	1.53855	−4.19069	25.2	5	−72.2	0.467
	$N = 3–2$, $J = 5/2–3/2$, $F = 2–2$	262.078935	0.20691	−5.06197	25.2	5	−85.5	0.063
H_2CO	$3_{03} - 2_{02}$	218.222192	16.29674	−3.55037	20.95640	7	0	1.000

Notes. The spectroscopic constants are taken from the CDMS database (Müller et al. 2001, 2005) for HCN, and from the JPL database (Pickett et al. 1998) for C_2H and H_2CO. Measurements are provided by Ahrens et al. (2002) for HCN, by Sastry et al. (1981) and Padovani et al. (2009) for C_2H, and by Bocquet et al. (1996) for H_2CO.
[a] Velocity shift from the brightest hyperfine component in the group.
[b] Relative intensity with respect to the brightest hyperfine component in the group.

(corresponding to linear spatial scales of 30–48 au) for the 1–0 lines. In addition to these fiducial images, we used a second set of images for the 3–2 lines, that were produced by applying a taper to match the resolution of the 1–0 lines (see Section 6.2 in Czekala et al. (2021), for a detailed description of how these images were produced). This set of maps are available on the MAPS project homepage.[24] The H_2CO line is weaker per beam than that of the other small organics, resulting in images with low S/N at high angular (0.″15) resolution. GM Aur is an exception here, as it presents bright H_2CO emission that is well-detected in the 0.″15 resolution image. For consistency, here we use the tapered version of the H_2CO images (with 0.″3 resolution) for all sources, which are more sensitive to low surface brightness and extended features. Disk integrated line fluxes for each line can be found in Table A1.

3. Spatial Distribution of the Emission

3.1. Zeroth-moment Maps

The velocity-integrated emission, or "zeroth-moment," maps of the HCN, C_2H, and H_2CO 3–2 and 1–0 lines are shown in Figure 1, where the dust continuum emission at 260 GHz (with ∼0.″1 angular resolution) is shown in the upper row for comparison. A description of the continuum emission images can be found in Sierra et al. (2021). For HCN $J = 3–2$ and $J = 1–0$, all hyperfine lines were included to generate the zeroth-moment maps, while for C_2H only the two brightest (and blended) lines are included in the $N = 3–2$ line, and the first and brightest component in the $N = 1–0$ line. For more details on the zeroth-moment map generation process, see Law et al. (2021a).

The 3–2 lines have higher fluxes than the lower-energy 1–0 lines for all disks. HCN $J = 3–2$ is strongly detected in all disks, and presents a variety of substructures, including central holes, single, and multiple rings. HCN $J = 1–0$ presents similar spatial distributions to the $J = 3–2$ line in AS 209, HD 163296, and MWC 480. Several rings are seen toward HD 163296, including a faint ring in the outer disk (centered at ∼400 au), far beyond the dust continuum edge. Toward IM Lup, the HCN $J = 1–0$ line emission is fainter and more extended than in the other disks, resulting in a lower-S/N zeroth-moment map. Toward GM Aur, the HCN $J = 1–0$ line is mostly detected in the central regions of the disk, although an outer diffuse ring is seen in the radial profile (see also Law et al. 2021a).

The C_2H $N = 3–2$ and $N = 1–0$ lines have spatial distributions and radial extents similar to HCN in AS 209, HD 163296, and MWC 480. Toward IM Lup and GM Aur, the $N = 3–2$ line is fainter than in the other disks, resulting in lower-S/N zeroth-moment maps, and the $N = 1–0$ line is mostly detected in the central regions of the disks, similar to HCN.

Fewer substructures are observed for H_2CO compared to HCN and C_2H, although a few ring-like structures are seen, in particular in HD 163296. The H_2CO line emission is more extended than HCN and C_2H, and presents a central hole of varying depths in all the disks except GM Aur and MWC 480, where only a tentative dip is observed. GM Aur presents exceptionally bright emission compared to the other disks.

Normally, for molecules other than ^{12}CO and ^{13}CO, it is not possible to derive the height of the emission directly from the spatially resolved image cubes (e.g., Rosenfeld et al. 2013; Pinte et al. 2018a). This is because other lines are typically fainter and arise in less elevated disk layers. However, thanks to the higher inclination and relative proximity of the HD 163296 disk, and the high angular resolution and sensitivity of the MAPS data, we can

[24] https://www.alma-maps.info

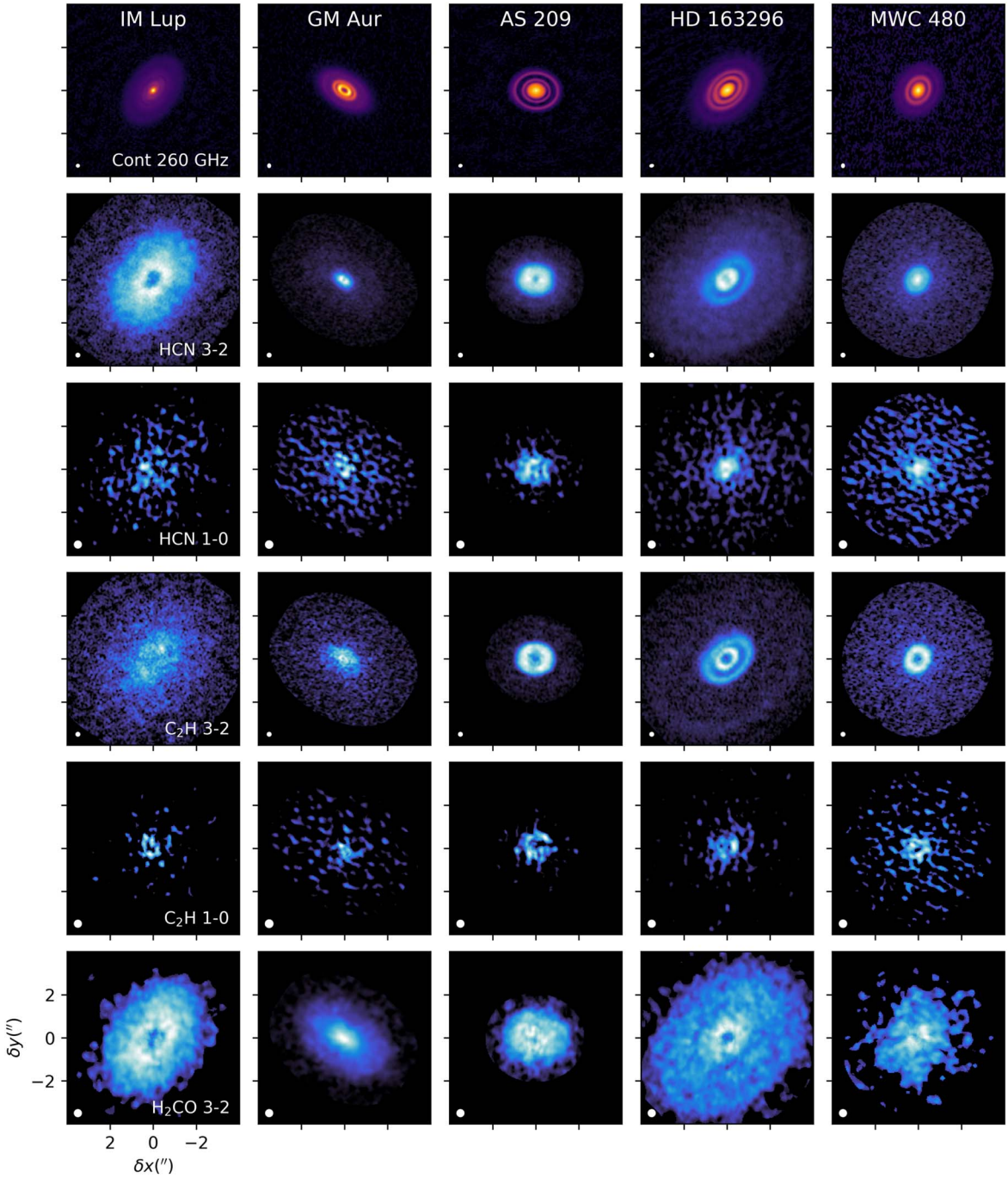

Figure 1. The 260 GHz dust continuum emission and zeroth-moment maps for the HCN $J = 3$–2 and $J = 1$–0, C_2H $N = 3$–2, $N = 1$–0, and H_2CO $J = 3$–2 lines. All the hyperfine components were included to generate the HCN zeroth-moment map, while only the brightest hyperfine component is included in the C_2H zeroth-moment map. The color is shown with power-law stretch to enhance the faint emission in the outer disk. The beam is shown in the bottom left corner of each panel.

distinguish emission arising in a flat disk from emission arising in the elevated layers above the disk midplane. Indeed, the HCN and C_2H 3–2 lines observed toward HD 163296 show a clear asymmetry along the disk minor axis that cannot be explained with emission from a flat disk. Part of the asymmetry, also seen as projected ellipses that look shifted to the south with respect to the disk center, is due to the fact that we are observing the emission from the near cone that is facing us. This effect is clearly seen in the zeroth-moment map, and corresponds to the heights estimated in Law et al. (2021b), i.e., $z/r \lesssim 0.1$. See Law et al. (2021b) for a detailed description of the emission surfaces for HCN and C_2H in the MAPS disk sample.

3.2. Radial Profiles

To better characterize the spatial distribution of the emission we used the `radial_profile` function of the Python package `GoFish` (Teague 2019) to produce deprojected radial intensity profiles from the zeroth-moment maps, considering the disk inclination and position angle (see Table 1). Although it is possible to take into account the vertical height of the emission to derive the radial intensity profiles (Law et al. 2021a), here we assume a flat disk but produce the deprojected profiles by averaging the emission within a 30° wedge along the disk major axis. The C_2H lines were not detected at sufficiently high

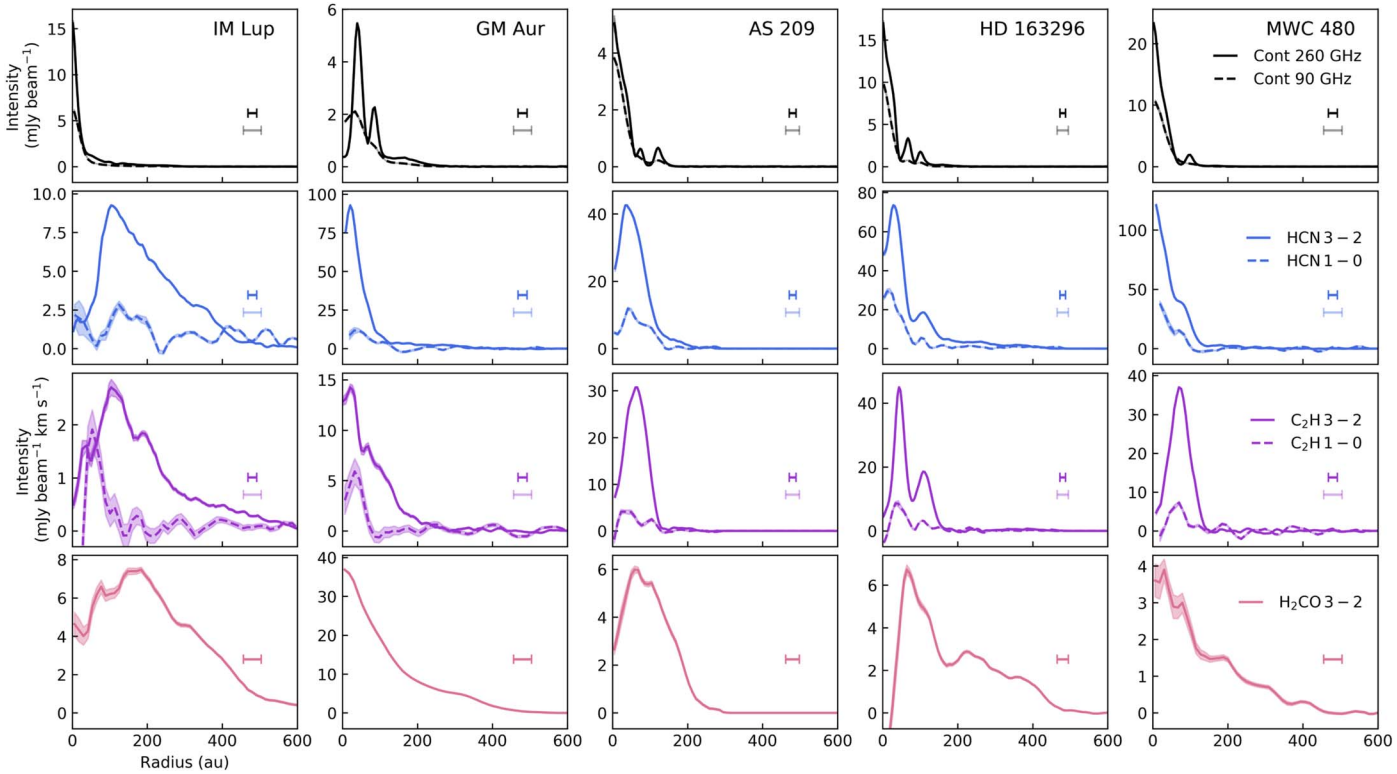

Figure 2. Deprojected radial intensity profiles of the continuum (first row), HCN (second row), C_2H (third row), and H_2CO (bottom row) emission lines. Solid and dashed lines correspond to the Band 6 and Band 3 observations, respectively. The horizontal bars mark the beam size of the observations, where light colors correspond to the Band 3 data. Color-shaded regions show the 1σ scatter at each radial bin divided by the square root of the ratio of bin circumference and FWHM of the synthesized beam (see Law et al. 2021a).

S/N toward IM Lup and GM Aur, so we averaged the emission azimuthally to produce the deprojected radial profiles. For additional details on the deprojected radial profiles, see Law et al. (2021a). The resulting profiles for the 3–2 (solid) and 1–0 (dashed) lines are shown in Figure 2. For comparison, the profiles of the 260 GHz and 90 GHz dust continuum emission are shown in the first row.

In general, the HCN and C_2H emission is more compact than that of H_2CO—their radial extents are smaller by a factor ∼2. Moreover, their radial extents are similar to that of the dust continuum emission, although faint HCN and C_2H emission is observed up to ∼400 au in HD 163296. IM Lup is an exception, as it presents similar radial extents in all molecular lines. One possibility to explain the lack of HCN and C_2H emission in the outermost disk regions where H_2CO is observed is that the H_2 gas density is not high enough to excite the lines. Indeed, for gas temperatures between 10 and 50 K, the HCN 3–2 line has a critical density of $(6–10) \times 10^6$ cm^{-3}, while the H_2CO 3–2 line has a critical density that is 10 times lower (Shirley 2015). However, models of these disks find that gas densities are $> 10^7$ cm^{-3} in the outer disk midplanes, enough to excite these lines (e.g., Zhang et al. 2021). This suggests that the abundance of HCN and C_2H decreases in the outermost disk regions where H_2CO is still abundant. We note that no additional emission arises in the outermost disk regions in the lower-resolution (0.″3) images that have better S/N.

The radial profiles are consistent with profiles previously observed at lower angular resolution (0.″5) for HCN and C_2H in IM Lup, AS 209, HD 163296, and MWC 480 (Bergner et al. 2019), and for H_2CO in all sources (Pegues et al. 2020). However, our higher-angular-resolution observations reveal additional radial substructures, in particular for HCN and C_2H. We focus on the 3–2 lines, which show more structure than the 1–0 lines due to the higher signal-to-noise ratios and angular resolution (see Law et al. 2021a, for additional substructure analysis).

3.2.1. HCN

HCN shows a central hole in four of five disks, the exception being MWC 480 where the emission is centrally peaked. A main ring of emission is seen for IM Lup, GM Aur, and AS 209, although the rings are not Gaussian but present one or more emission shoulders that could result from blended ring components not resolved in the MAPS data. IM Lup shows an unusually broad, almost plateau-like ring. Two bright rings are seen for HD 163296, centered at ∼30 and 110 au, and a fainter plateau that extends up to ∼400 au. In addition, a shallow gap is seen at ∼327 au along with a faint ring centered at ∼366 au (Law et al. 2021a). The ring is better seen in the zeroth-moment map (see Figure 1). GM Aur and AS 209 also present faint HCN emission in the outer disk. In addition to the central emission component, MWC 480 shows an emission shoulder at ∼30 au, and a partially blended ring at ∼90 au (see also Law et al. 2021a). HCN radial profiles observed at similar linear spatial resolution toward other disks around T Tauri stars generally show centrally peaked emission profiles with emission bumps in the outer disk (e.g., Hily-Blant et al. 2019; Kastner et al. 2018).

3.2.2. C_2H

C_2H shows a central hole for all disks, which is generally larger than the hole seen for HCN. Several unresolved ring

components are seen toward IM Lup and GM Aur, similar to what is observed in HCN. AS 209 presents a single ring of C_2H emission, very similar in size to the ring seen in HCN. Two rings are seen toward HD 163296, centered roughly at the same locations of the HCN rings. The two faint HCN rings seen in the outer disk are also observed for C_2H in the zeroth-moment map (see Figure 1), but are harder to see in the radial profiles. The presence of these faint C_2H outer rings is confirmed with the tapered (0.″3 resolution) image, which has higher S/N (Law et al. 2021a). Toward MWC 480, a single C_2H ring is observed centered at the same location of the outermost HCN ring. Interestingly, the innermost C_2H ring seen in HD 163296 and the rings seen in AS 209 and MWC 480 are all located near a gap in the dust continuum emission. Similar ring-like structures with large central cavities have been observed for C_2H toward other disks, like TW Hya (Bergin et al. 2016) and V4046 Sgr (Kastner et al. 2018).

3.2.3. H_2CO

H_2CO radial profiles present more complicated substructure, such as broad ring-like emission components with several shoulders and/or local maxima. In the inner disk, IM Lup, AS 209, and HD 163296 present a central depression in H_2CO emission, while GM Aur and MWC 480 show centrally peaked emission profiles. In the outer disks (>100 au), the slope at which the H_2CO intensity decreases is much more shallow compared to HCN and C_2H, in particular for the disks around HD 163296 and MWC 480.

The radial profiles show spatial links between H_2CO substructures, namely line emission peaks, and the outer edge of the millimeter continuum disk. H_2CO peaks are aligned with the outer edge of the continuum in IM Lup and HD 163296. Additionally, the higher-resolution (0.″15) images of AS 209, as noted in Law et al. (2021a), also show the presence of an additional H_2CO ring that is radially coincident with the dust edge. Toward HD 163296, a spatial link between a H_2CO line emission peak and outer dust edge was seen in lower-resolution data from Carney et al. (2017). Spatial links between millimeter dust edges and H_2CO line emission have also been observed toward other disks, like TW Hya (Öberg et al. 2017) and V4046 Sgr (Kastner et al. 2018), as well as in four out of a sample of 15 disks in the survey presented by Pegues et al. (2020). All MAPS disks were included in those surveyed by Pegues et al. (2020), but a close association between an outer H_2CO ring and millimeter dust edge in the MAPS disks, as reported here, was not clearly seen in Pegues et al. (2020), due to these outer H_2CO rings not being clearly spatially resolved. Thus, when considering these previous survey results with the new MAPS observations, this suggests that at least ∼50% of disks may show some spatial links between H_2CO substructures and the outer edge of the continuum disk.

In summary, we find some similarities between the HCN and C_2H radial profiles. Furthermore, several of the H_2CO peaks spatially coincide with the HCN and C_2H peaks, for example the first H_2CO peak seen toward AS 209. However, most of the H_2CO features do not have direct counterparts in HCN or C_2H, and the H_2CO radial extents are larger.

4. Column Densities

To derive column density profiles, we first produce deprojected spectra at different radii using the `radial_spectra` function of `GoFish`. The radial bins are set to 1/4 of the beam major axis, and the disk is assumed to be vertically flat. Before averaging the spectra in each radial bin, the velocity is shifted according to the Keplerian rotation of the disk, so that all the spectra are aligned. The stellar masses needed to compute the Keplerian velocities are taken from Öberg et al. (2021) and are estimated from gas dynamics in Teague et al. (2021). The spectra are azimuthally averaged in those disks with low S/N (C_2H for IM Lup and GM Aur, and H_2CO for all sources), and averaged within a 30° wedge along the disk major axis for the others. The main motivation for using a 30° wedge when possible is to avoid the uncertainty of the emission surface height, which strongly influences the spatial location of emission near the minor axis.

4.1. Column Density Retrieval

To derive the column densities, we assume that the emission is in local thermal equilibrium (LTE) and that the emission fills the beam. The LTE assumption is reasonable, considering the high densities present in protoplanetary disks. Cataldi et al. (2021) performed a non-LTE fit to the HCN lines and found similar column densities, suggesting our LTE assumption is a good approximation, at least for HCN. The line intensity is computed as

$$I_\nu = (B_\nu(T_{\rm ex}) - B_\nu(T_{\rm bg}))[1 - \exp(-\tau_\nu)], \quad (1)$$

where B_ν is the Planck function, $T_{\rm ex}$ is the excitation temperature, $T_{\rm bg}$ is the background temperature, and τ_ν is the line optical depth. The background temperature $T_{\rm bg}$ is fixed to the maximum of the continuum brightness temperature or the cosmic microwave background (CMB) temperature (2.73 K).

At the line center, the optical depth is given by

$$\tau_0 = \frac{A_{ul} c^3 N_u}{8\pi\nu^3\sigma\sqrt{2\pi}}\left[\exp\left(\frac{h\nu}{kT_{\rm ex}}\right) - 1\right], \quad (2)$$

where A_{ul} is the Einstein coefficient, ν is the frequency of the line, σ is the Gaussian line width, and N_u is the upper-level column density,

$$N_u = \frac{N_{\rm tot}}{Q(T_{\rm ex})} g_u \exp\left(\frac{-E_u}{kT_{\rm ex}}\right). \quad (3)$$

Here, $N_{\rm tot}$ corresponds to the total column density of the molecule, g_u is the upper-level degeneracy, E_u is the upper-level energy, and $Q(T_{\rm ex})$ is the partition function. The spectroscopic constants and partition functions were taken from the CDMS and JPL catalogs and are listed in Table 2.

The free parameters in the fit are the total column density $N_{\rm tot}$, the FWHM $\Delta V = 2\sqrt{2\ln 2}\,\sigma$, and the excitation temperature in the case of HCN and C_2H, as their lines present hyperfine structure. For H_2CO, the excitation temperature is fixed because only a single line is available. We also allow for a small offset from the source velocity $v_{\rm lsr}$, constrained between −0.25 and 0.25 km s^{-1}. We explore the parameter space using the `emcee` package (Foreman-Mackey et al. 2013). The best fit is taken as the 50th percentile of the samples in the marginalized distributions, and the associated errors are computed from the 16th and 84th percentiles.

4.2. HCN and C_2H Fitting Method

We follow a method similar to the one implemented in Bergner et al. (2019). The HCN and C_2H lines present hyperfine structure that is spectrally resolved. We fit the observed spectra assuming that all the hyperfine lines have the same excitation temperature. Each hyperfine line is assumed to be a Gaussian, such that the total line opacity is given by

$$\tau_\nu = \sum_i \tau_0 r_i \exp\left(-\frac{(v - v_i - v_{\rm lsr})^2}{2\sigma^2}\right), \quad (4)$$

where $\tau_{i,0}$ is the line center opacity of the ith component, v_i is the relative velocity of each component with respect to the brightest line, and $v_{\rm lsr}$ is the source velocity. The relative intensities r_i as well as the relative velocities v_i are listed in Table 2.

The width of spectral lines is dominated by thermal broadening, which depends on the gas temperature:

$$\sigma_{\rm therm} = \sqrt{\frac{k{\rm T}_{\rm gas}}{m}}, \quad (5)$$

where m is the molecule's mass. Under the assumption of LTE, $T_{\rm gas} = T_{\rm ex}$. However, we find that the observed line widths for HCN and C_2H are broader than their thermal widths would imply. This is most likely produced by beam smearing, where line emission from different radii in the disk that have different velocities are combined in a single beam. In addition to beam smearing, it is possible that emission from both the back and front sides of the flared disk, which have slightly different projected velocities, are being combined in the observed spectra. The inner disk is particularly affected by these issues, which makes it difficult to fit the lines without artificially decreasing the line opacity or increasing the excitation temperature. A way to alleviate this problem is to first compute the line intensity assuming a purely thermal line width, then compute the total flux, and finally redistribute this flux in the line but now for the observed and broader line width. With this method, the fit to the lines is better, and the inferred line opacity—and hence the column density—is more realistic. The same solution was applied to fit the CN and DCN lines in the MAPS disks (Bergner et al. 2021; Cataldi et al. 2021).

The fit to the observed spectra was done in two steps. First, we fit the 1–0 and 3–2 lines simultaneously to obtain a better constraint on the excitation temperature. The tapered (0.″3) versions of the 3–2 line cubes were used for this step, to match the resolution of the 1–0 line cubes. We included priors on the excitation temperature informed by the gas temperature traced by the optically thick ^{12}CO 2–1 line. Law et al. (2021b) found that the HCN and C_2H emission arises from relatively flat surfaces $z/r \lesssim 0.1$ in AS 209, HD 163296, and MWC 480, while the CO isotopologues arise in more elevated disk layers. We thus restrict the rotational temperature between 10 K and the gas temperature inferred from the peak brightness temperature of the optically thick ^{12}CO 2–1 line, $T_{\rm gas}(^{12}{\rm CO})$ (Law et al. 2021b), for both HCN and C_2H. The results for the simultaneous fit to the 1–0 and 3–2 lines are shown in Appendix B. The resulting excitation temperature and column density profiles are shown in Figure B1, and the gray curves show the $T_{\rm gas}(^{12}{\rm CO})$ profiles for each disk. HCN presents rotational temperatures between 15 and 40 K, while C_2H presents higher values of 15–60 K. The column densities are on the order of 10^{13}–$10^{15}{\rm cm}^{-2}$ for both molecules. Despite the lower angular resolution of 0.″3 of the data used in these analyses, two column density rings are resolved in both HCN and C_2H for HD 163296, and a single ring or central component for the other sources.

In the second step, and to obtain a better-resolved column density profile, we fit the high-angular-resolution 3–2 lines only. We used the excitation temperature found in the previous step ($T_{\rm ex,0}$) as an initial parameter, and constrain $T_{\rm ex,0} - 10\,{\rm K} < T_{\rm ex} < T_{\rm ex,0} + 10\,{\rm K}$ for both HCN and C_2H. Figure 3 shows a selection of observed spectra and fit for each species and disk. Note that the radial extent is different for each disk. The lines are fit well in most of the disk, but poorly fit in the inner disk, where the lines are substantially broader, resulting in the individual hyperfine components being completely blended. For this reason, we used the ^{12}CO or ^{13}CO temperature as the excitation temperature in regions where the fit does not work properly. For C_2H, the $T_{\rm gas}(^{12}{\rm CO})$ was used for all sources. For HCN, the $T_{\rm gas}(^{12}{\rm CO})$ was used for IM Lup, GM Aur, and AS 209. For the two disks around Herbig Ae stars, however, the $T_{\rm gas}(^{13}{\rm CO})$ was used instead, since the $T_{\rm gas}(^{12}{\rm CO})$ produced a large discontinuity in the column density profile.

An independent retrieval of the HCN column density and excitation temperature is presented in Bergner et al. (2021) and Cataldi et al. (2021), using a method similar to the one presented here but with different constraints on the excitation temperature. A comparison between the HCN column densities presented in these three papers is shown in Appendix C. The resulting column density profiles and excitation temperatures are consistent with the ones presented here (see Figure C1).

4.3. H_2CO Fitting Method

For H_2CO, we fit a single Gaussian to the $J = 3$–2 line in each radial bin. In order to constrain the H_2CO excitation temperature, a combination of lines with different upper level energies is needed. Since we only observed one line, the excitation temperature is fixed and the column density was computed for a range of excitation temperatures between 20 and 50 K so that we are not a priori assuming the vertical location of the H_2CO emitting layer. The range of temperatures is based on previous estimates. For example, Pegues et al. (2020) recently showed that the bulk H_2CO emission in four Class II disks arises in 11–40 K gas, using multi-line H_2CO observations with similar energy ranges ($E_u = 20$–70 K). In particular, for MWC 480 they found a low excitation temperature of ∼21 K. Similarly, toward HD 163296 the disk-averaged H_2CO excitation temperature has been estimated to be ∼24 K (Carney et al. 2017; Guzmán et al. 2018). Finally, toward the older (∼8 Myr; Sokal et al. 2018) TW Hya disk, Terwisscha van Scheltinga et al. (2021) recently found that H_2CO emits mostly from a 30–40 K layer, corresponding to an elevated disk layer of $z/r \geqslant 0.25$.

We found that the column density is not very sensitive to $T_{\rm ex}$; the difference in column density is only a factor ∼2 for this range of temperatures. The observed spectra with the best-fit overlaid are shown in the bottom panels in Figure 3. As was found for HCN and C_2H, the lines are fit well in most of the disk, but poorly fit in the inner ∼30 au, especially in HD 163296 and MWC 480. This is probably due to contamination from the back side of the disk.

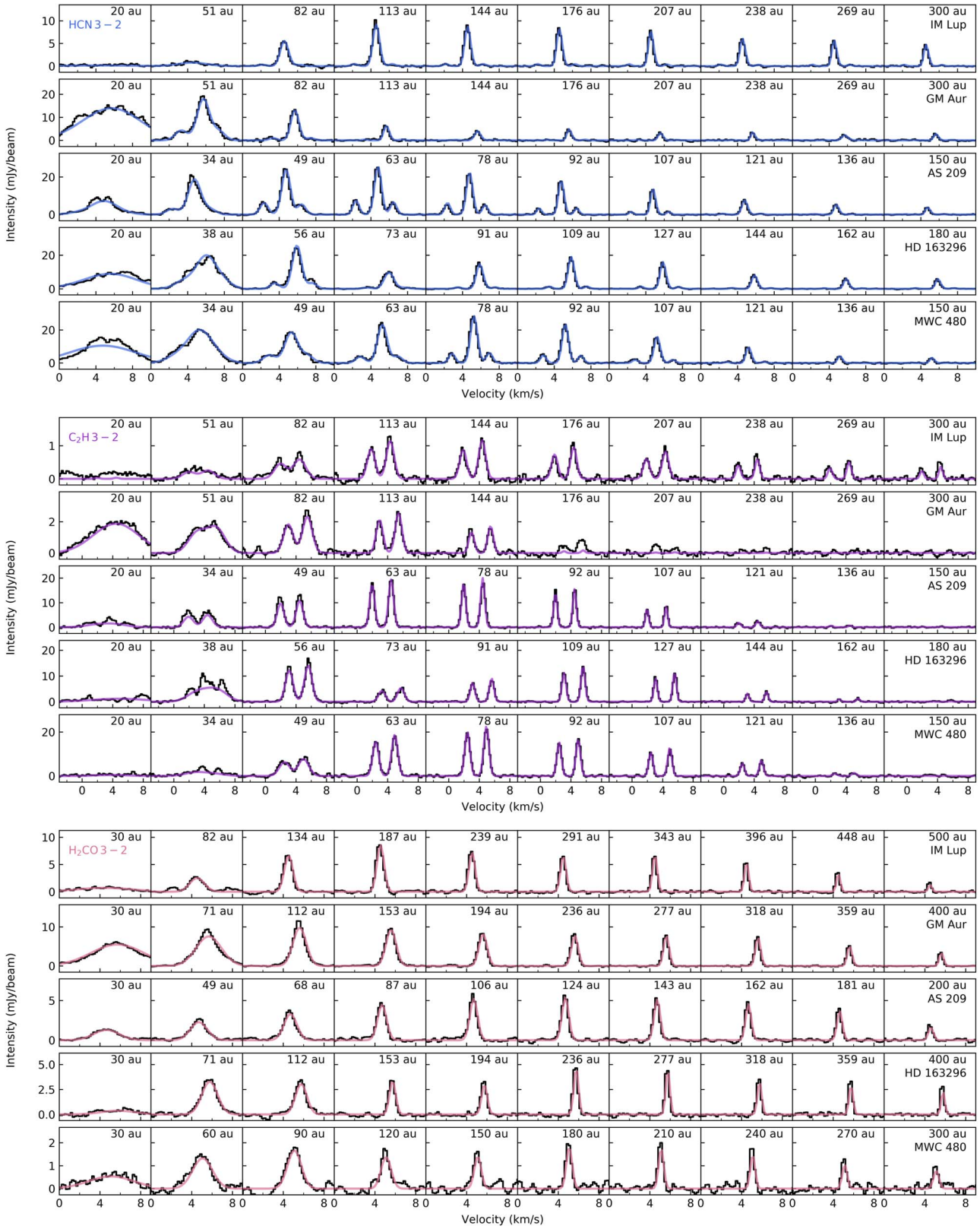

Figure 3. Deprojected spectra averaged over radial annuli for HCN (top), C_2H (middle), and H_2CO (bottom) lines. The observed spectra are shown in black, and the best-fit are shown in color. For H_2CO, the best-fit model for a temperature of 20 K is shown. The radius of the center of each radial bin is shown at the top of each panel.

4.4. HCN, C_2H, and H_2CO Column Density Profiles

The resulting column density profiles for HCN, C_2H, and H_2CO are shown in Figure 4. Two profiles are shown for H_2CO, corresponding to T_{ex} of 20 and 50 K. The gray shaded area marks the inner regions where $T_{gas}(^{12}CO)$ or $T_{gas}(^{13}CO)$ was used as the excitation temperature in the fit. The horizontal bars show the spatial resolution of the profiles for each molecule and disk.

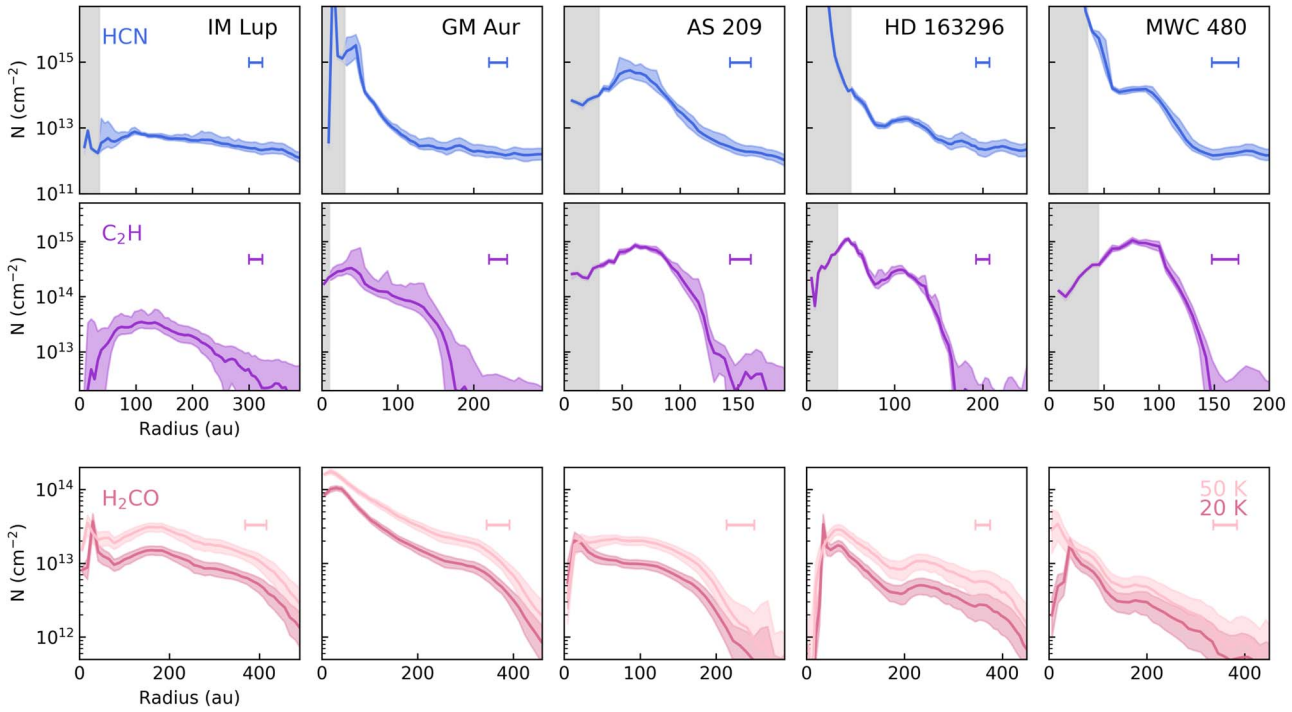

Figure 4. Column density profiles for HCN (top), C_2H (middle), and H_2CO (bottom). The horizontal bar at the upper right marks the spatial resolution of the profiles. Gray shaded areas mark the regions where the excitation temperature was assumed to be equal to the ^{12}CO or ^{13}CO temperature. Two column density profiles are shown for H_2CO, assuming a fixed excitation temperature of 20 and 50 K.

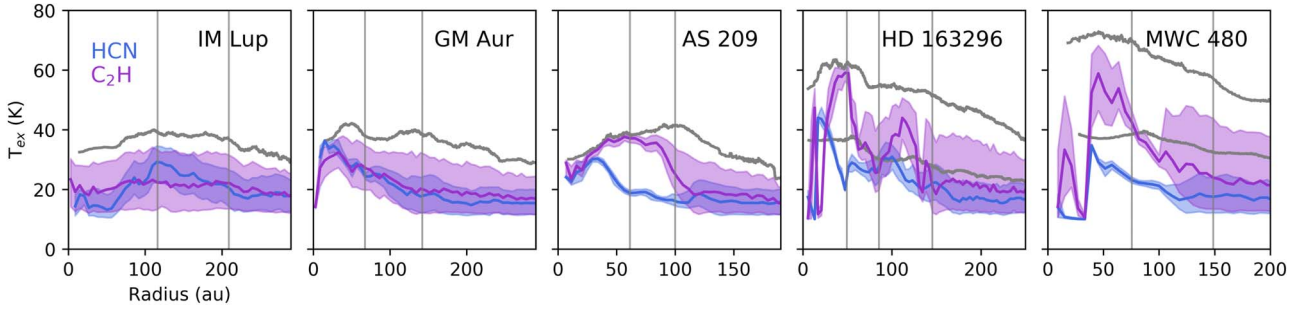

Figure 5. Excitation temperatures for HCN and C_2H derived from the fit to the 3–2 lines only. The $T_{gas}(^{12}CO)$ temperature is shown in gray for all sources. In addition, the $T_{gas}(^{13}CO)$ temperature is shown for HD 163206 and MWC 480. The horizontal bar at the upper right marks the resolution of the profiles. The gray vertical lines show the position of the gaps seen in the dust millimeter continuum as measured by Law et al. (2021a).

The HCN and C_2H column densities range from 10^{12} to 10^{15} cm^{-2}, although the HCN column density may reach $\gtrsim 10^{16} cm^{-2}$ in the inner 30 au of GM Aur, HD 163296, and MWC 480. Overall, HCN and C_2H present similar column density profiles, except for that HCN has a central component in GM Aur, HD 163296, and MWC 480, while the inner disk seems to be depleted of C_2H in all sources but toward GM Aur. GM Aur presents a central dust cavity (see Figure 2), which could result in enhanced C_2H abundance in the inner disk. However, there is evidence that the total H_2 gas is also depleted inside the dust cavity (Dutrey et al. 2008; Huang et al. 2020; Bosman et al. 2021b). Another difference between HCN and C_2H is in the outer >150 au disk. The HCN column density seems to reach a plateau of a few times $10^{12} cm^{-2}$, which is not present for C_2H.

The H_2CO column density profiles are consistent with the ones derived by Pegues et al. (2020) for all sources using different H_2CO transitions and at lower angular resolution. H_2CO is present at higher column density at larger disk radii compared to HCN and C_2H. Although the spatial resolution for the H_2CO column density profiles is lower than for the smaller organics, a few distinct rings can be seen in the profiles. GM Aur and AS 209 present less structure, while at least two rings or local maxima are seen for HD 163296 and MWC 480. The H_2CO column density varies between the sources, ranging between 10^{12} and 10^{14} cm^{-2} in the inner 200 au. The largest column densities are seen toward GM Aur and IM Lup, which together with AS 209 are the coldest disks in the sample if we consider their stellar mass and the large disk masses that have been estimated (Cleeves et al. 2016; McClure et al. 2016).

4.5. HCN and C_2H Excitation Temperatures

Figure 5 shows the excitation temperature profiles inferred for HCN and C_2H from fitting the higher-angular-resolution 3–2 lines only, informed by the T_{ex} obtained from the simultaneous fit to the 1–0 and 3–2 lines. The $T_{gas}(^{12}CO)$ and $T_{gas}(^{13}CO)$ profiles are shown in gray. At least for 3/5 sources, the C_2H excitation temperatures are higher than those derived for HCN. HCN temperatures range from 20 to 30 K, while C_2H

temperatures range from 20 to 60 K. The C_2H excitation temperatures in the outer disk regions (>100 au) of AS 209, HD 163296, and MWC 480 are consistent with the temperatures derived by Bergner et al. (2019) at lower angular resolution. Excitation temperatures for HCN do not vary substantially within the disk sample. However, the inferred T_{ex} values for C_2H are higher for HD 163296 and MWC 480 than for the other three disks. This is consistent with disks around Herbig Ae stars being warmer than disks around lower-mass T Tauri stars, and suggest that C_2H arises in warmer elevated disk layers compared to HCN.

The inferred excitation temperatures are low (20–30 K) for both HCN and C_2H in IM Lup and GM Aur, and do not vary substantially across the disks. Toward AS 209, the C_2H excitation temperature profile shows a ring-like distribution similar to the column density ring seen in Figure 4, reaching a peak $T_{ex} \sim 40$ K in one of the dust gaps. HCN, on the other hand, shows a decreasing T_{ex} profile with radius. Toward HD 163296, the C_2H and HCN excitation temperatures show two rings, similar to the distribution of the column densities, although the rings are more pronounced for C_2H than for HCN. Toward MWC 480, the T_{ex} of HCN and C_2H decrease with radius in a smoother profile compared to HD 163296. Finally, in AS 209 and HD 163296, the T_{ex} peaks of C_2H spatially coincide with the column density peaks. We do not find the same correlation for the other sources or for HCN.

5. Discussion

5.1. Location of the HCN and C_2H Emission Surfaces

Chemical models predict HCN and C_2H emission arises in elevated disk layers where UV photons drive the gas to temperatures of 40–50 K and dominate the chemistry (Bergin et al. 2016; Cleeves et al. 2018). However, a recent analysis of observations toward a sample of 16 disks at lower (>0.″5) angular resolution resulted in low excitation temperatures of 5–10 K and 10–40 K for HCN and C_2H, respectively (Bergner et al. 2019). Bergner et al. (2019) suggested that the origin of the lower-than-expected excitation temperatures could be due to subthermal emission or beam dilution due to unresolved chemical substructure. The higher-angular-resolution MAPS data reveals these substructures across a sample of disks for the first time. In addition, the 1–0 line observations now allow us to better constrain the molecular excitation temperature. While we do find HCN excitation temperatures that are higher than inferred by Bergner et al. (2019) toward these disks, they remain relatively low (<30 K). For C_2H, on the other hand, we find higher excitation temperatures that are more consistent with the gas temperature at the expected height of the emission, in particular for the warmer disks HD 163296 and MWC 480, which are also disks that present the most substructure in their emission.

The inferred excitation temperatures for HD 163296 are consistent with the brightness temperature distributions of the HCN and C_2H 3–2 lines found by Law et al. (2021b). These brightness temperatures provide a lower limit to the gas temperature because these lines are partly optically thin. These results, combined with the emission heights estimated by Law et al. (2021b) of $z/r \lesssim 0.1$, suggest that the HCN emission arises in vertically deeper and colder layers than C_2H.

For IM Lup and GM Aur, the T_{ex} of C_2H and HCN are very similar, which suggests that their emission arises from similar disk layers. However, given our uncertainties, we cannot rule out a vertical stratification. Indeed, detailed chemical models of IM Lup suggest that HCN arises in deeper layers compared to C_2H. (Cleeves et al. 2018). Finally, it is worth mentioning that the C_2H excitation temperature is lower for the colder disks around T Tauri stars, which show fewer substructures compared to the disks around Herbig Ae stars. This could be due to intrinsic lower gas temperatures or to small-scale substructure not resolved in our observations.

5.2. Comparison to CO Column Densities

CO is widely used to trace the gas in disks because H_2 does not have strong transitions in the low temperature range that characterizes disks. Thus, we compare the column density profiles of the small organics with that of CO. Figure 6 shows the normalized column density profiles of HCN, C_2H, and H_2CO, as well as the CO column densities derived from the $C^{18}O$ 2–1 line by Zhang et al. (2021). In general, the HCN and CO column densities tend to be more centrally peaked than that of C_2H, suggestive of an active warm cyanide chemistry in the inner disk. In the outer disk, HCN and C_2H show similar radial distributions up to ~150 au, where the C_2H column density starts to drop faster than HCN and CO. There is notably good spatial correlation between the profiles toward HD 163296 between $50 < r < 150$ au.

In general, the HCN and CO column densities correlate well, except in AS 209, where significant differences are observed. In particular, an anticorrelation is observed between CO and both HCN and C_2H. Alarcón et al. (2021) used chemical models to investigate the gas structure in AS 209, and showed that this anticorrelation can be explained by CO chemical processing, which produces a decrease in the CO abundance and an elevated C/O ratio (>2) in the gas that boosts the formation of C_2H. Bosman et al. (2021a) also found that elevated C/O ratios (~2) are needed to explain the observed C_2H column densities for AS 209, MWC 480, and HD 163296. C_2H is therefore very sensitive to the gas-phase C/O abundance ratio in the disk atmosphere (Bergin et al. 2016; Cleeves et al. 2018; Miotello et al. 2019).

5.3. Photochemistry of HCN and C_2H

If the formation of HCN and C_2H is the result of a UV-dominated chemistry, we might expect to see enhanced column densities inside the dust gaps. The depletion of millimeter dust at these locations should allow the deeper penetration of UV photons, and thus efficient formation of C_2H and HCN. However, the penetration of UV photons will also depend on the geometry of the source (for example, the flaring of the disk). It is nevertheless worth comparing the structures observed in mm dust and molecular emission. The position of the dust continuum gaps, as measured by Law et al. (2021a) (but see references therein), are marked by the gray dashed vertical lines in Figure 6. We only include the gaps that are resolved at ~0.″1 resolution. However, several other gaps are seen in higher-angular-resolution observations of the dust continuum emission (Huang et al. 2018, 2020). The peak of the C_2H column density seen toward IM Lup, AS 209, MWC 480, and the first peak seen toward HD 163296, coincides with the location of the innermost dust gaps, although the C_2H structures are generally broad compared to the dust gaps. The second column density peak seen at ~110 au toward HD 163296 does not spatially coincide with any of the dust gaps,

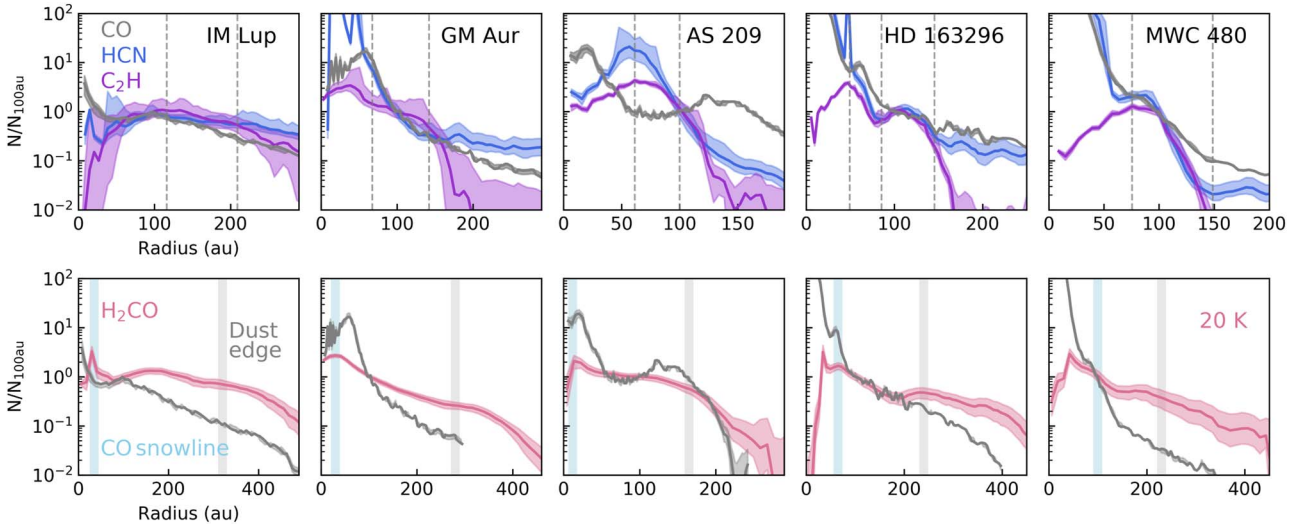

Figure 6. Normalized column density profiles for HCN, C_2H (top), and H_2CO (bottom). For comparison, the CO column density profiles are shown in gray (Zhang et al. 2021). The vertical dashed lines show the position of the gaps seen in the dust continuum as measured by Law et al. (2021a). The light blue vertical lines mark the estimated location of the CO snowline (Zhang et al. 2021). The light gray vertical lines mark the edge of the millimeter dust disk.

revealing that there is not a universal connection between dust depletion and C_2H or HCN formation. The weak correlation between dust structures and HCN and C_2H chemical substructures could be due to the HCN and C_2H emission arising in disk elevated layers, which are not always impacted by the dust millimeter substructure that trace the midplane. Moreover, recent studies have shown that the H_2 density seems to be much less altered than the dust inside the dust gaps, and chemical effects play a more important role in setting molecular abundances (e.g., Teague et al. 2018b; Alarcón et al. 2021; Zhang et al. 2021).

If photochemistry drives the formation of HCN and C_2H, we could also expect to see enhanced emission in the outer disk where the gas density starts to drop allowing UV photons to penetrate the disk. The flaring of the outer disk could also help to capture more UV photons from the star. Although the HCN and C_2H emission is compact compared to H_2CO, some faint emission is indeed detected at large radii, far beyond the dust millimeter edge in IM Lup, GM Aur, and HD 163296. As an example, Figure 7 shows radial structures seen in the tapered images for HD 163296, the disk that presents the most substructure in molecular line emission. A power-law stretch was used in the *y*-axis, to enhance the low-S/N structure seen in the outer disk. A faint ring that is seen in both HCN and C_2H near 400 au is also seen in CN (Bergner et al. 2021). The ring is not clearly seen in H_2CO in the radial profile, but a ring structure is visible at large radii in the zeroth-moment map, in particular along the disk minor axis (see Figure 1). No millimeter dust grains are present at these larger radii, but small dust grains are present, as suggested by scattered light images (e.g., Monnier et al. 2017; Avenhaus et al. 2018; Rich et al. 2020). A small dust grain population is also present in the disk elevated layers where HCN and C_2H emission seems to arise. This small grain population is likely regulating the HCN and C_2H chemistry. An increased amount of UV photons will also contribute to enhanced HCN destruction in the outer disk. Indeed, Bergner et al. (2021) find an increasing CN/HCN profile with radius, indicative of increased HCN photodissociation relative to CN in the lower-density outer disk (see also Guzmán et al. 2015). All this suggests that an active photochemistry is at play in the outer disk beyond the millimeter dust emission around HD 163296. Even so, as mentioned in the previous section, the C/O ratio in the gas may still be more important than UV exposure for the formation of HCN and C_2H in the outer disk.

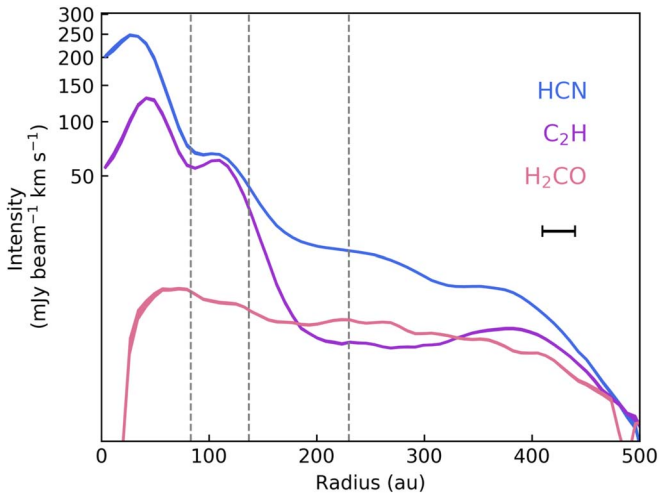

Figure 7. Deprojected radial profiles of the HCN, C_2H, and H_2CO 3–2 lines toward HD 163296. The profiles are computed from the tapered 0.″3 images. The dashed vertical lines mark the position of the putative planets at 83, 137, and 230 au (Teague et al. 2018a; Pinte et al. 2018b).

5.4. Links to Planet Formation

Several efforts have been made in recent years to find planets forming in protoplanetary disks. The presence of several planets has been proposed to explain the gaps seen in the dust continuum emission and the deviation from Keplerian rotation in CO observed in a few disks, including HD 163296 (Teague et al. 2018a; Pinte et al. 2018b, 2020; Teague et al. 2021) and MWC 480 (Teague et al. 2021). While dust depletion in the midplane can be inferred from the millimeter dust continuum observations, it has been harder to infer the gaps are also depleted in gas, since all millimeter lines, including CO isotopologues, may reflect chemistry variations rather than true gas density variations. Indeed, chemistry has a nonlinear response to gas density. see Rab et al. (2020) for detailed thermochemical modeling of HD 163296

in particular. Here, we compare the locations of the planets proposed for HD 163296 and MWC 480 with the structures observed in HCN, C_2H, and H_2CO.

In Figure 7, we compare the emission of HCN, C_2H, and H_2CO with the locations of the putative planets in HD 163296 (dashed vertical lines). Besides the two bright rings seen in the inner 150 au, two fainter rings are resolved in the outer disk for both HCN and C_2H (see also Law et al. 2021a). The planet predicted at 83 au by Teague et al. (2018a) and Isella et al. (2016) is located inside a dust millimeter gap, which coincides with the gap seen in HCN and C_2H. This gap is also recovered in the column density profiles (Figure 4). The correlation between the planet location and a decrease in the C_2H column density was previously hinted by Bergner et al. (2019). Although the gaps seen for HCN and C_2H are much shallower than what is observed for the millimeter dust, these observations suggest the gap is also depleted of gas.

Toward MWC 480, Teague et al. (2021) proposed that a planet near 245 au could explain the observed CO deviations from Keplerian rotation. However, HCN and C_2H are not detected at these large radii. At smaller radii (<200 au), no perturbations could be confirmed in the CO gas kinematics. However, a gap is seen in HCN at around 70 au, which roughly corresponds to the location of a millimeter dust gap. The gap is not seen in C_2H. Hydrodynamical simulations suggest that a $\sim$2.3 M_J planet located at an orbital radius of $\sim$78 au could produce the observed dust gap (Liu et al. 2019). If there is a corresponding gas gap, then this suggests that HCN may be more sensitive to gas density perturbations than C_2H, and could potentially be used as a diagnostic to identify massive planets in protoplanetary disks.

5.5. Origin of the H_2CO Emission

H_2CO could be a better tracer of the colder gas in the outer disk than HCN and C_2H, which seem to trace warmer elevated layers in the disks. The use of H_2CO as a tracer of cold gas depends on its dominant formation pathway and on the efficiency of desorption mechanisms. H_2CO can form from both gas-phase and grain surface chemistry. The dominant reaction in the gas phase at low ($\lesssim$100 K) temperatures is the neutral–neutral reaction

$$CH_3 \xrightarrow{O} H_2CO. \quad (6)$$

The grain surface chemistry pathway involves the successive hydrogenation of CO ices (Hidaka et al. 2004; Watanabe et al. 2004; Fuchs et al. 2009)

$$CO \xrightarrow{H} HCO \xrightarrow{H} H_2CO \xrightarrow{H} H_3CO \xrightarrow{H} CH_3OH. \quad (7)$$

This pathway can only be efficient in regions where CO has started to freeze out onto dust grains, i.e., beyond the CO snowline and below and around the CO snow surface, depending on whether the CO hydrogenation is faster than the CO desorption. The light blue vertical lines in the bottom panels of Figure 6 mark the estimated location of the CO snowline in each disk as measured by Zhang et al. (2021). CO snowlines are located at smaller radii in the colder disks around T Tauri stars, compared to the warmer HD 163296 and MWC 480 disks, where the CO snowline is well-resolved by our observations. The first H_2CO ring seen toward HD 163296 and MWC 480 spatially coincides with the estimated location of the CO snowline, suggesting that CO hydrogenation is an important (if not dominant) formation pathway of H_2CO in disks.

In the warm inner disk, H_2CO is expected to form mainly in the gas phase, since CO cannot freeze out onto dust grains. The inner regions of the MAPS disks all show central H_2CO depressions, although they are less pronounced for GM Aur and AS 209. This does not mean that H_2CO is depleted in the inner disk; it could purely be a result of the observed line being more sensitive to cold gas. Indeed, higher-energy lines have shown centrally peaked emission profiles suggesting a warmer H_2CO component is present in the inner disk (Loomis et al. 2015; Öberg et al. 2017).

In the outer disk, both gas-phase and CO hydrogenation could contribute to the overall H_2CO emission. In Section 3.2.3, we showed that at least $\sim$50% of disks may show some spatial links between H_2CO substructures and the outer edge of the continuum disk. We also observe spatial links between the H_2CO column density profiles and the outer edge of the continuum disk, which are marked by the gray vertical lines in Figure 6. In particular, the second ring or bump component seen in the H_2CO column density profiles of HD 163296 and MWC 480 spatially coincides with the millimeter dust edge. A similar coincidence is seen toward IM Lup and GM Aur, where a shoulder-type structure is seen near the continuum edge. This suggests that the release of ices at large distances becomes more efficient, either through thermal desorption due to thermal inversion (Cleeves 2016), or via nonthermal desorption due to the penetration of UV photons (e.g., Podio et al. 2020; van't Hoff et al. 2020). Another possibility is that other ice fragments are released into the gas phase in the outer disk, which then boost the gas-phase chemistry enhancing the abundance of H_2CO.

The H_2CO traced by our observations could also form predominantly in the gas phase through reaction (6), with little contribution from the CO hydrogenation pathway (7). This could happen if nonthermal desorption of H_2CO ices is not efficient and H_2CO remains frozen onto dust grains. In this scenario, the emission would arise in more elevated and warmer disk layers. Although chemical models have shown that pure gas-phase chemistry cannot account for the observed H_2CO abundances in the outer disk around DM Tau (Loomis et al. 2015), observations of edge-on Class I disks have shown that H_2CO emission arises in the warmer surface layers, as revealed by X-shaped patterns in their zeroth-moment maps (Podio et al. 2020; van't Hoff et al. 2020). These observations, however, targeted the H_2CO 3_{12}–2_{11} line which has a relatively large upper-level energy of $\sim$33 K, and is therefore more sensitive to the warmer elevated disk layers. Lower-energy lines could trace colder gas present at intermediate disk layers. In order to confirm the origin of the H_2CO emission, multi-line observations are needed (e.g., Pegues et al. 2020). The results toward Class II disks found by Pegues et al. (2020) suggest a possible trend between the location of the H_2CO emitting layer and the age of the disk, or perhaps a difference between disks around T Tauri and Herbig stars. Future multiline observations toward a larger sample of disks with a consistent set of lines may help to elucidate whether this trend is real.

5.6. Small Organics Reservoir in the Inner 50 au

We can estimate the amount of HCN, C_2H, and H_2CO present in the inner disk regions. The gas masses within 50 au are listed in Table 3. Because of the uncertainties of the fit in the inner disk, we extrapolated the column density profiles

Table 3
Small Organic Reservoir in the Inner 50 au

Source	Gas Mass			Gas+Ice Mass w.r.t. H_2O Ice[a]		
	HCN (10^{22} g)	C_2H (10^{22} g)	H_2CO (10^{22} g)	HCN (% H_2O)	C_2H (% H_2O)	H_2CO (% H_2O)
IM Lup	0.03	0.05	0.20	<0.001	<0.001	0.001
GM Aur	19.63	2.04	0.79	0.56	0.06	0.02
AS 209	1.99	3.27	0.15	1.09	1.80	0.08
HD 163296	46.36	6.03	0.24	0.68	0.09	0.004
MWC 480	59.92	2.17	1.21	0.45	0.02	0.01

Note.
[a] Assuming an ice-to-gas ratio of 1000.

inward, assuming a constant column density starting from the radius where we obtain a good fit (see Figure 4). This means that the HCN masses estimated for GM Aur, HD 163296, and MWC 480, which tend to have centrally peaked N profiles, could be larger than what we have estimated here. The total amount of HCN, C_2H, and H_2CO is, however, much larger because a large fraction of the organic reservoir is expected to reside in icy mantles. Indeed, as discussed before, the emission of these small organics arises in disk layers with temperatures of 20–60 K, which are lower than the freeze-out temperature of these molecules. Assuming a conservative ice-to-gas ratio of 1000 (these ratios could be larger, as discussed in Öberg et al. 2021), we find a large amount (10^{23}–10^{26} g) of gas phase plus ice mantle HCN, C_2H, and H_2CO in the inner disks. Interestingly, the relative amounts of these organics varies between the disks. For example, H_2CO is ∼5 times more abundant than HCN and C_2H in IM Lup, while H_2CO is less abundant than HCN and C_2H in the rest of the disks. HCN is more abundant (by a factor ∼10–50) than both C_2H and H_2CO in GM Aur, HD 163296, and MWC 480, and AS 209 has a slightly larger C_2H mass than HCN.

We can also compare the amount of organics with respect to water ice in these disks. The total water mass inside 50 au was estimated from the models presented in Zhang et al. (2021), and are listed in Table 1 of Öberg et al. (2021). The abundance of total gas and ice HCN, C_2H, and H_2CO relative to water are listed in the right columns of Table 3. The fractions range from 0.5% to 1.1% and 0.02% to 1.8% for HCN and C_2H, respectively, not taking into account IM Lup, which has much lower organic fractions of <0.001%. The fractions for H_2CO are lower, ranging from 0.001% to 0.08%. Typical abundances with respect to water in cometary ices range from 0.1% to 0.6% for HCN and from 0.1% to 1% for H_2CO (Mumma & Charnley 2011), which are consistent with our organic fraction estimates.

The MAPS disks are therefore rich in organic species, suggesting that future comets formed in these disks could efficiently deliver water and other key organics to rocky planets forming in the inner disk.

6. Conclusions

We have presented spatially resolved observations of the small organics HCN, C_2H, and H_2CO toward a sample of five protoplanetary disks from the MAPS program. The main conclusions are the following:

1. The line emission reveals substantial substructure, in particular toward the warmer disks around HD 163296 and MWC 480, where several rings are observed in HCN and C_2H.
2. We derive column density profiles and find the distributions vary across disks, suggesting that the specific physical conditions in each disk play a major role in setting the organic distribution in disks.
3. We find similarities between the HCN and C_2H distribution in the outer disk regions, suggesting a similar chemistry drives their formation, most likely photochemistry in the temperate disk layers.
4. The HCN and C_2H excitation temperatures, estimated by the 1–0 and 3–2 lines as well as the hyperfine structure of the lines, range between 20 and 60 K. The temperatures are higher for C_2H, however, suggesting that the HCN emission arises in a colder and deeper layer than C_2H, and is thus more sensitive to density variations.
5. HD 163296 and MWC 480 show gaps in their HCN column density profiles, which spatially coincide with the location of planets suggested in previous studies. This opens the possibility of using HCN to trace gas density variations in disks, and finding the massive planets that could be carving these gaps.
6. Contrary to HCN and C_2H, H_2CO emits from a much more extended region of the disks, far beyond the dust millimeter edge. H_2CO is slightly more abundant in the colder disks around T Tauri stars than in disks around Herbig stars, but is particularly abundant in the GM Aur disk.
7. We find enhanced H_2CO column densities at the CO snowline location and another column density enhancement around the millimeter dust edge.
8. We estimated the total gas plus ice mass inside 50 au for the MAPS disks, and find large amounts (10^{23}–10^{26} g) of organic material, with fractions with respect to water ice that are consistent with fractions observed in comets of our solar system.

We have shown that high-angular-resolution (down to ∼10 au) and high-sensitivity observations from these small organics provide a window into the C, O, and N budget of disks. The inner 50 au regions of the MAPS disks are rich in organic species, so comets forming in these disks could potentially deliver water and other key organics to nascent rocky planets. Future observations toward other disks with different stellar masses, ages, and disk properties will provide a more complete picture of the organic reservoir in disks, and the impact these properties may have on the possible outcomes of planet formation.

We thank the anonymous referee for valuable comments that improved this manuscript.

This paper makes use of the following ALMA data: ADS/JAO.ALMA#2018.1.01055.L. ALMA is a partnership of ESO (representing its member states), NSF (USA) and NINS (Japan), together with NRC (Canada), MOST and ASIAA (Taiwan), and KASI (Republic of Korea), in cooperation with the Republic of Chile. The Joint ALMA Observatory is operated by ESO, AUI/NRAO and NAOJ. The National Radio Astronomy Observatory is a facility of the National Science Foundation operated under cooperative agreement by Associated Universities, Inc.

V.V.G. acknowledges support from FONDECYT Iniciación 11180904 and ANID project Basal AFB-170002. J.B.B. acknowledges support from NASA through the NASA Hubble Fellowship grant No. HST-HF2-51429.001-A, awarded by the Space Telescope Science Institute, which is operated by the Association of Universities for Research in Astronomy, Inc., for NASA, under contract NAS5-26555. G.C. is supported by NAOJ ALMA Scientific Research grant code 2019-13B. C.J.L. acknowledges funding from the National Science Foundation Graduate Research Fellowship under grant DGE1745303. K.I.Ö acknowledges support from the Simons Foundation (SCOL No. 321183). K.I. Ö, E.A.B, F.A., and A.D.B. acknowledge support from NSF AAG grant No. 1907653. C.W. acknowledges financial support from the University of Leeds, STFC, and UKRI (grant Nos. ST/R000549/1, ST/T000287/1, and MR/T040726/1). Y.A. acknowledges support by NAOJ ALMA Scientific Research grant code 2019-13B, and Grant-in-Aid for Scientific Research 18H05222 and 20H05847. S.M.A. and J.H. acknowledge funding support from the National Aeronautics and Space Administration under grant No. 17-XRP17 2-0012 issued through the Exoplanets Research Program. I.C. was supported by NASA through the NASA Hubble Fellowship grant HST-HF2-51405.001-A awarded by the Space Telescope Science Institute, which is operated by the Association of Universities for Research in Astronomy, Inc., for NASA, under contract NAS5-26555. J.H. acknowledges support for this work provided by NASA through the NASA Hubble Fellowship grant No. HST-HF2-51460.001-A awarded by the Space Telescope Science Institute, which is operated by the Association of Universities for Research in Astronomy, Inc., for NASA, under contract NAS5-26555. K.Z. acknowledges the support of the Office of the Vice Chancellor for Research and Graduate Education at the University of Wisconsin–Madison with funding from the Wisconsin Alumni Research Foundation, and the support of NASA through Hubble Fellowship grant HST-HF2-51401.001. awarded by the Space Telescope Science Institute, which is operated by the Association of Universities for Research in Astronomy, Inc., for NASA, under contract NAS5-26555. R.L.G. acknowledges support from a CNES fellowship grant. J.D.I. acknowledges support from the Science and Technology Facilities Council of the United Kingdom (STFC) under ST/T000287/1. R.T. acknowledges support from the Smithsonian Institution as a Submillimeter Array (SMA) Fellow. L.I.C. gratefully acknowledges support from the David and Lucille Packard Foundation and Johnson & Johnson's WiSTEM2D Program. F.L. acknowledges support from the Smithsonian Institution as a Submillimeter Array (SMA) Fellow. K.R.S. acknowledges the support of NASA through the NASA Hubble Fellowship grant No. HST-HF2-51419.001 awarded by the Space Telescope Science Institute, which is operated by the Association of Universities for Research in Astronomy, Inc., for NASA, under contract NAS5-26555. L.M.P. acknowledges support from ANID project Basal AFB-170002 and from ANID FONDECYT Iniciación project No. 11181068. F.M. acknowledges support from ANR of France under contract ANR-16-CE31-0013 (Planet-Forming-Disks) and ANR-15-IDEX-02 (through CDP "Origins of Life"). Y.L. acknowledges the financial support by the Natural Science Foundation of China (grant No. 11973090).

Software: Astropy (Astropy Collaboration et al. 2013; Price-Whelan et al. 2018), CASA (McMullin et al. 2007), `GoFish` (Teague 2019), NumPy (van der Walt et al. 2011), SciPy (Virtanen et al. 2020).

Appendix A
Disk-integrated Line Fluxes

The disk-integrated line fluxes and upper limits for the observed HCN, C_2H, and H_2CO lines are listed in Table A1. For HCN and C_2H, the integrated line fluxes include several hyperfine components that are blended in velocity. The fluxes were computed using elliptical masks that were constructed using the disk inclinations and position angles listed in Table 1, and an outer radius based on the observed extent of the emission of each line. The uncertainties were estimated by computing integrated fluxes using the same elliptical mask but centered at 500 random positions that are free from line emission in the map. The listed uncertainties correspond to the standard deviation of these line-free integrated fluxes.

Table A1
HCN, C_2H, and H_2CO Disk-integrated Lines Fluxes

Molecule	Line	IM Lup (mJy km s^{-1})	GM Aur (mJy km s^{-1})	AS 209 (mJy km s^{-1})	HD 163296 (mJy km s^{-1})	MWC 480 (mJy km s^{-1})
HCN	$J = 1$–0, $F = 1$–1; $F = 2$–1; $F = 0$–1	88.3 ± 14.4	113.4 ± 14.8	226.8 ± 15.9	736.3 ± 58.3	138.6 ± 19.6
	$J = 3$–2, $F = 3$–2; $F = 3$–3; $F = 2$–2	2343.7 ± 86.3	1814.6 ± 130.5	2940.8 ± 71.7	7043.3 ± 459.3	2494.4 ± 122.8
C_2H	$N = 1$–0, $J = 3/2$–1/2, $F = 2$–1	<30	<16	60.7 ± 9.7	130.1 ± 34.2	44.3 ± 17.2
	$N = 1$–0, $J = 3/2$–1/2, $F = 1$–0	<8	<13.9	40.1 ± 11.9	56.1 ± 14.1	<15.1
	$N = 3$–2, $J = 7/2$–5/2, $F = 4$–3; $F = 3$–2	430.8 ± 59.3	294.2 ± 97.9	1716.6 ± 56.7	2527.5 ± 223.1	1076.4 ± 66.6
	$N = 3$–2, $J = 5/2$-3/2, $F = 3$–2; $F = 2$–1	620.2 ± 88.3	506.7 ± 102.0	2119.7 ± 73.9	3230.6 ± 400.4	1418.0 ± 72.7
	$N = 3$–2, $J = 5/2$-3/2, $F = 2$–2	<37	<77	142.4 ± 33.8	188.4 ± 69.4	36.3 ± 18.2
H_2CO	$3_{03} - 2_{02}$	752.2 ± 72.1	900.0 ± 56.7	292.5 ± 27.9	813.4 ± 78.1	144.5 ± 38.9

Appendix B
Simultaneous Fit to the 3–2 and 1–0 Lines

Figure B1 shows the HCN and C_2H column density and excitation temperature profiles found when fitting the 1–0 and 3–2 lines simultaneously. The spatial resolution of the profiles is 0.″3, which corresponds to the resolution of the tapered version of the 1–0 line images. An example with the resulting best-fit spectra found for AS 209 are shown in Figure B2. The weakest C_2H 3–2 hyperfine line listed in Table 2 and shown in the bottom panel of the figure is detected in all disks except IM Lup.

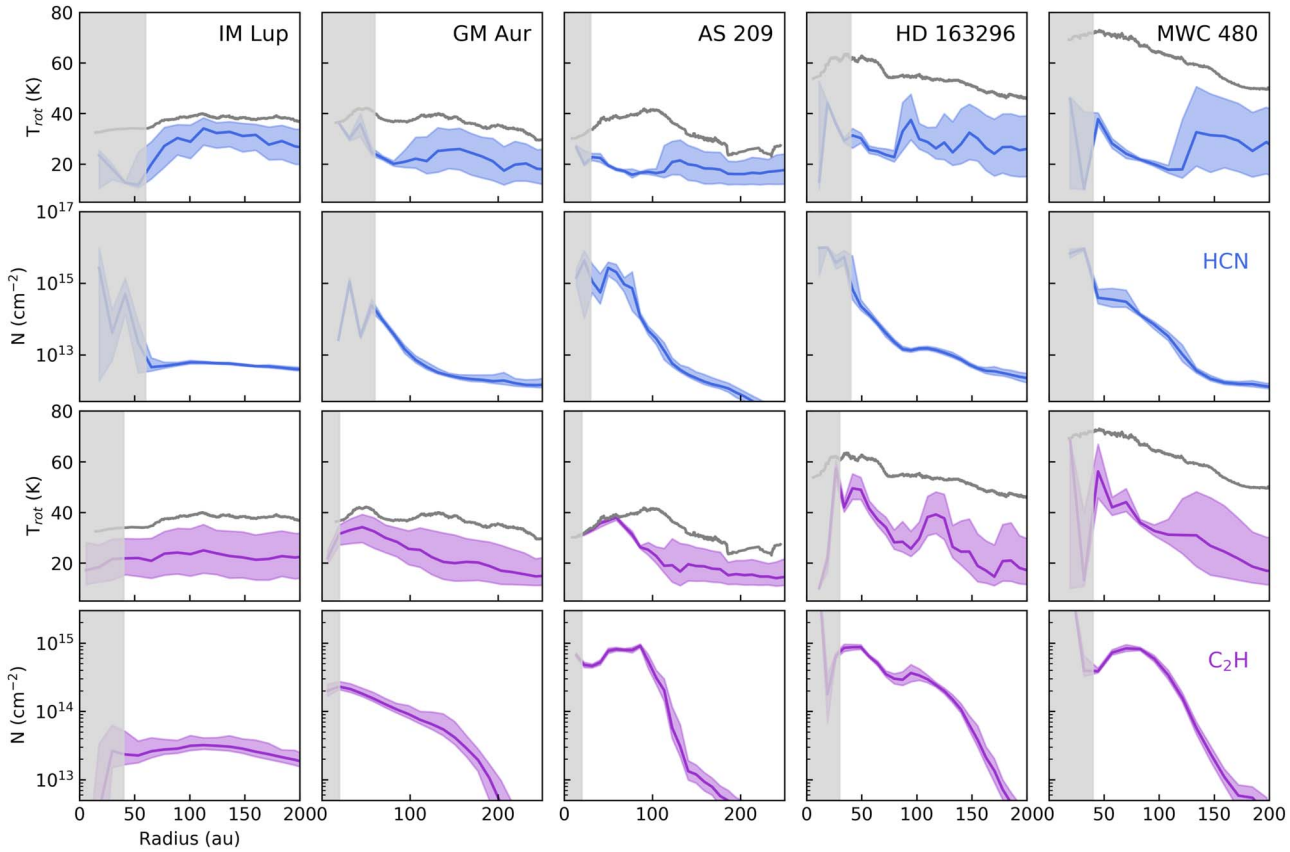

Figure B1. Best-fit rotational temperature and column density profiles to the 1–0 and 3–2 lines. The two upper and two bottom rows correspond to HCN and C_2H, respectively. The gray curves correspond to the gas temperatures derived from the optically thick ^{12}CO 2–1 line (Law et al. 2021b) and was used as the maximum rotational temperature allowed in the fit. Gray shaded areas mark the regions where the lines are poorly fit. The resolution of the profiles is 0.″3.

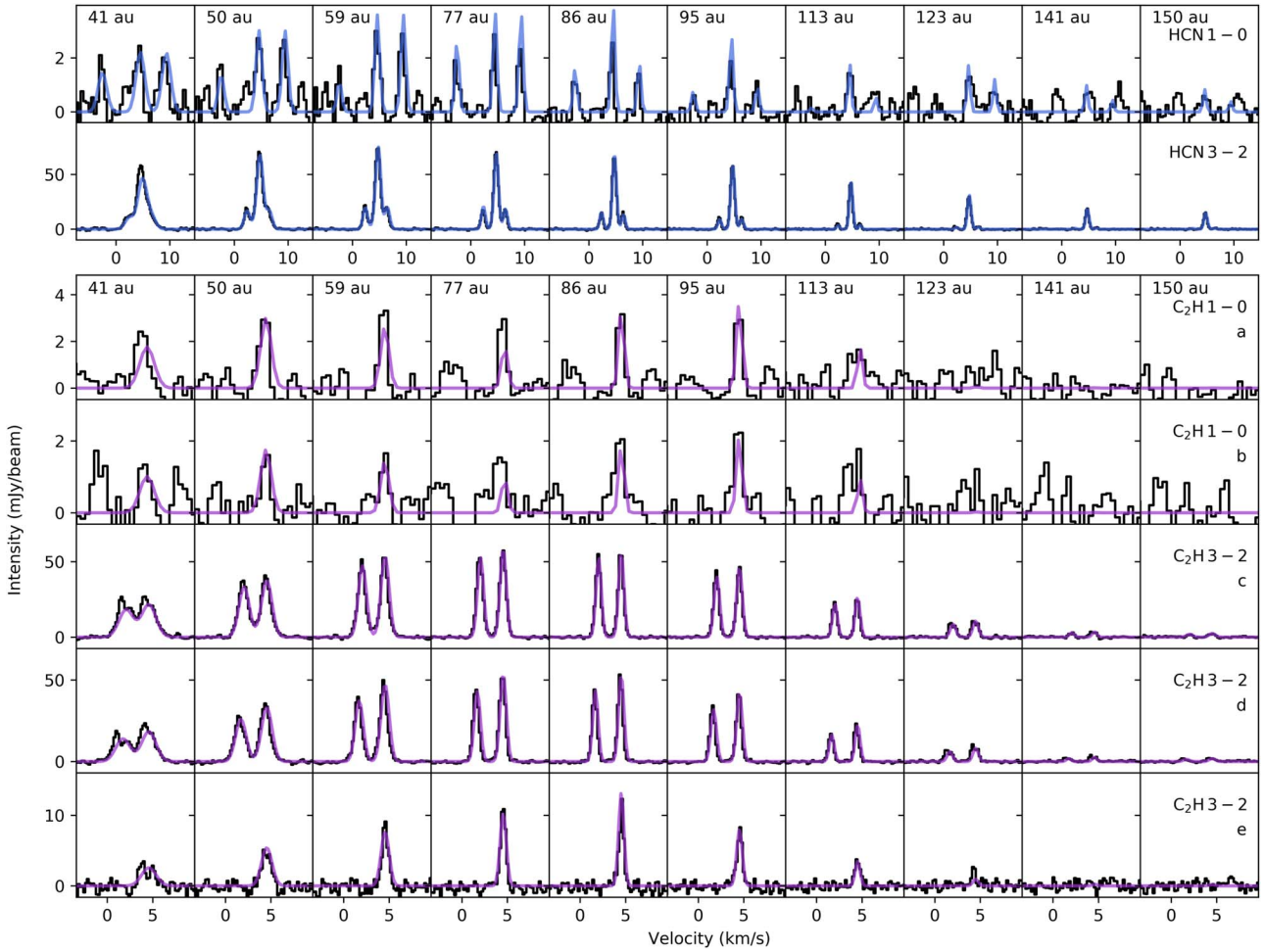

Figure B2. Deprojected spectra averaged over radial annuli in AS 209. HCN and C_2H lines are shown in the top and bottom panels, respectively. The 3–2 lines correspond to the tapered images with $0\farcs3$ resolution. The observed spectra are shown in black, and the best-fit are shown in color. Several hyperfine lines are shown for C_2H: (a) and (b) correspond to the $F = 2$–1 and $F = 1$–0 components of the 1–0 line; (c) corresponds to the $F = 4$–3 and $F = 3$–2 components associated with the $J = 7/2$–$5/2$ group of the 3–2 line; (d) corresponds to the $F = 3$–2 and $F = 2$–1 components associated with the $J = 5/2$-$3/2$ group of the 3–2 line; and (e) corresponds to the $F = 2$–2 component associated with the $J = 5/2$–$3/2$ group of the 3–2 line.

Appendix C
Comparison of HCN Column Density Profiles

The MAPS data were used to derive HCN column density profiles in two other papers. Bergner et al. (2021) derived CN and HCN column density profiles using a column density retrieval method similar to the one presented here. Cataldi et al. (2021) also derived HCN column density profiles, but using the lower-angular-resolution images because the goal was to compare them to the profiles of DCN. The Band 6 DCN line is faint and was not detected at high S/N in the high-angular-resolution images. The resulting HCN column density profiles from these different analyses are shown in Figure C1. The profiles are consistent for all disks, and differences are only observed in the inner disk where the fit is known to behave poorly.

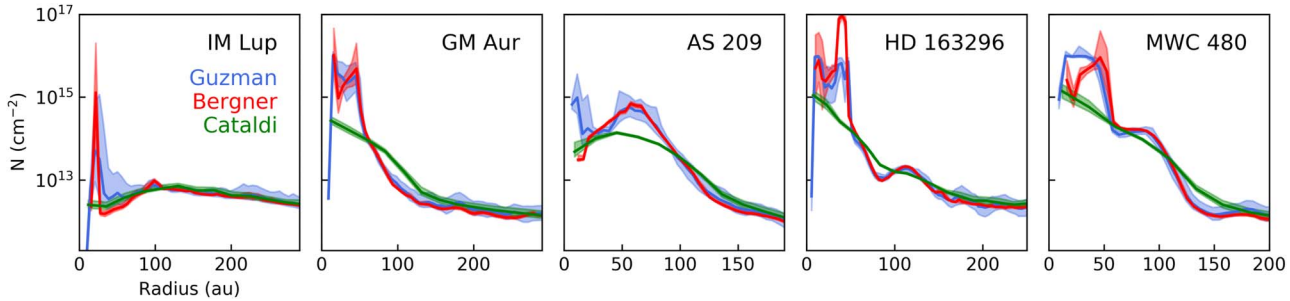

Figure C1. Column density profiles for HCN derived from this work (blue), Bergner et al. (2021) (red), and Cataldi et al. (2021) (green).

ORCID iDs

Viviana V. Guzmán https://orcid.org/0000-0003-4784-3040
Jennifer B. Bergner https://orcid.org/0000-0002-8716-0482
Charles J. Law https://orcid.org/0000-0003-1413-1776
Karin I. Öberg https://orcid.org/0000-0001-8798-1347
Catherine Walsh https://orcid.org/0000-0001-6078-786X
Gianni Cataldi https://orcid.org/0000-0002-2700-9676
Yuri Aikawa https://orcid.org/0000-0003-3283-6884
Edwin A. Bergin https://orcid.org/0000-0003-4179-6394
Ian Czekala https://orcid.org/0000-0002-1483-8811
Jane Huang https://orcid.org/0000-0001-6947-6072
Sean M. Andrews https://orcid.org/0000-0003-2253-2270
Ryan A. Loomis https://orcid.org/0000-0002-8932-1219
Ke Zhang https://orcid.org/0000-0002-0661-7517
Romane Le Gal https://orcid.org/0000-0003-1837-3772
Felipe Alarcón https://orcid.org/0000-0002-2692-7862
John D. Ilee https://orcid.org/0000-0003-1008-1142
Richard Teague https://orcid.org/0000-0003-1534-5186
L. Ilsedore Cleeves https://orcid.org/0000-0003-2076-8001
David J. Wilner https://orcid.org/0000-0003-1526-7587
Feng Long https://orcid.org/0000-0002-7607-719X
Kamber R. Schwarz https://orcid.org/0000-0002-6429-9457
Arthur D. Bosman https://orcid.org/0000-0003-4001-3589
Laura M. Pérez https://orcid.org/0000-0002-1199-9564
François Ménard https://orcid.org/0000-0002-1637-7393
Yao Liu https://orcid.org/0000-0002-7616-666X

References

Ahrens, V., Lewen, F., Takano, S., et al. 2002, ZNatA, 57, 669
Aikawa, Y., Momose, M., Thi, W.-F., et al. 2003, PASJ, 55, 11
Alarcón, F., Bosman, A. D., Bergin, E. A., et al. 2021, ApJS, 257, 8
Andrews, S. M. 2020, ARA&A, 58, 483
Andrews, S. M., Huang, J., Pérez, L. M., et al. 2018, ApJL, 869, L41
Astropy Collaboration, Robitaille, T. P., Tollerud, E. J., et al. 2013, A&A, 558, A33
Avenhaus, H., Quanz, S. P., Garufi, A., et al. 2018, ApJ, 863, 44
Becker, S., Feldmann, J., Wiedemann, S., et al. 2019, Sci, 366, 76
Bergin, E. A., Du, F., Cleeves, L. I., et al. 2016, ApJ, 831, 101
Bergin, E. A., Hogerheijde, M. R., Brinch, C., et al. 2010, A&A, 521, L33
Bergner, J., Öberg, K. I., Guzmán, V. V., et al. 2021, ApJS, 257, 11
Bergner, J. B., Guzmán, V. G., Öberg, K. I., Loomis, R. A., & Pegues, J. 2018, ApJ, 857, 69
Bergner, J. B., Öberg, K. I., Bergin, E. A., et al. 2019, ApJ, 876, 25
Bocquet, R., Demaison, J., Poteau, L., et al. 1996, JMoSp, 177, 154
Bosman, A. D., Alarcón, F., Bergin, E. A., et al. 2021a, ApJS, 257, 7
Bosman, A. D., Bergin, E. A., Loomis, R. A., et al. 2021b, ApJS, 257, 15
Carney, M. T., Hogerheijde, M. R., Loomis, R. A., et al. 2017, A&A, 605, A21
Carney, M. T., Hogerheijde, M. R., Guzmán, V. V., et al. 2019, A&A, 623, A124
Cataldi, G., Yamato, Y., Aikawa, Y., et al. 2021, ApJS, 257, 10
Cazzoletti, P., van Dishoeck, E. F., Visser, R., Facchini, S., & Bruderer, S. 2018, A&A, 609, A93
Chapillon, E., Dutrey, A., Guilloteau, S., et al. 2012, ApJ, 756, 58
Chuang, K. J., Fedoseev, G., Qasim, D., et al. 2017, MNRAS, 467, 2552
Cleeves, L. I. 2016, ApJL, 816, L21
Cleeves, L. I., Bergin, E. A., & Harries, T. J. 2015, ApJ, 807, 2
Cleeves, L. I., Bergin, E. A., O'D. Alexander, C. M., et al. 2016, ApJ, 819, 13
Cleeves, L. I., Öberg, K. I., Wilner, D. J., et al. 2018, ApJ, 865, 155
Czekala, I., Loomis, R. A., Teague, R., et al. 2021, ApJS, 257, 2
Du, F., Bergin, E. A., & Hogerheijde, M. R. 2015, ApJL, 807, L32
Du, F., Bergin, E. A., Hogerheijde, M., et al. 2017, ApJ, 842, 98
Dutrey, A., Guilloteau, S., Piétu, V., et al. 2008, A&A, 490, L15
Favre, C., Fedele, D., Semenov, D., et al. 2018, ApJL, 862, L2
Foreman-Mackey, D., Hogg, D. W., Lang, D., & Goodman, J. 2013, PASP, 125, 306
Fuchs, G. W., Cuppen, H. M., Ioppolo, S., et al. 2009, A&A, 505, 629
Guzmán, V. V., Öberg, K. I., Carpenter, J., et al. 2018, ApJ, 864, 170
Guzmán, V. V., Öberg, K. I., Loomis, R., & Qi, C. 2015, ApJ, 814, 53
Henning, T., & Semenov, D. 2008, in IAU Symp. 251, Organic Matter in Space, ed. S. Kwok & S. Sanford (Cambridge: Cambridge Univ. Press), 89
Hidaka, H., Watanabe, N., Shiraki, T., Nagaoka, A., & Kouchi, A. 2004, ApJ, 614, 1124
Hily-Blant, P., Magalhaes de Souza, V., Kastner, J., & Forveille, T. 2019, A&A, 632, L12
Hogerheijde, M. R., Bergin, E. A., Brinch, C., et al. 2011, Sci, 334, 338
Huang, J., Öberg, K. I., Qi, C., et al. 2017, ApJ, 835, 231
Huang, J., Andrews, S. M., Dullemond, C. P., et al. 2018, ApJL, 869, L42
Huang, J., Andrews, S. M., Dullemond, C. P., et al. 2020, ApJ, 891, 48
Isella, A., Guidi, G., Testi, L., et al. 2016, PhRvL, 117, 251101
Kastner, J. H., Qi, C., Dickson-Vandervelde, D. A., et al. 2018, ApJ, 863, 106
Law, C., Loomis, R. A., Teague, R., et al. 2021a, ApJS, 257, 3
Law, C., Teague, R., Loomis, R. A., et al. 2021b, ApJS, 257, 4
Liu, Y., Dipierro, G., Ragusa, E., et al. 2019, A&A, 622, A75
Long, F., Pinilla, P., Herczeg, G. J., et al. 2018, ApJ, 869, 17
Loomis, R. A., Cleeves, L. I., Öberg, K. I., et al. 2018, ApJ, 859, 131
Loomis, R. A., Cleeves, L. I., Öberg, K. I., Guzman, V. V., & Andrews, S. M. 2015, ApJL, 809, L25
Mathews, G. S., Klaassen, P. D., Juhász, A., et al. 2013, A&A, 557, A132
McClure, M. K., Bergin, E. A., Cleeves, L. I., et al. 2016, ApJ, 831, 167
McMullin, J. P., Waters, B., Schiebel, D., Young, W., & Golap, K. 2007, in ASP Conf. Ser., 376, ed. R. A. Shaw, F. Hill, & D. J. Bell (San Francisco, CA: ASP), 127
Miotello, A., Facchini, S., van Dishoeck, E. F., et al. 2019, A&A, 631, A69
Monnier, J. D., Harries, T. J., Aarnio, A., et al. 2017, ApJ, 838, 20
Müller, H. S. P., Schlöder, F., Stutzki, J., & Winnewisser, G. 2005, JMoSt, 742, 215
Müller, H. S. P., Thorwirth, S., Roth, D. A., & Winnewisser, G. 2001, A&A, 370, L49
Mumma, M. J., & Charnley, S. B. 2011, ARA&A, 49, 471
Najita, J. R., Carr, J. S., Pontoppidan, K. M., et al. 2013, ApJ, 766, 134
Najita, J. R., Carr, J. S., Salyk, C., et al. 2018, ApJ, 862, 122
Öberg, K. I., & Bergin, E. A. 2021, PhR, 893, 1
Öberg, K. I., Guzmán, V. V., Furuya, K., et al. 2015, Natur, 520, 198
Öberg, K. I., Guzmán, V. V., Walsh, C., et al. 2021, ApJS, 257, 1
Öberg, K. I., Qi, C., Fogel, J. K. J., et al. 2011, ApJ, 734, 98
Öberg, K. I., Guzmán, V. V., Merchantz, C. J., et al. 2017, ApJ, 839, 43
Padovani, M., Walmsley, C. M., Tafalla, M., Galli, D., & Müller, H. S. P. 2009, A&A, 505, 1199
Patel, B. H., Percivalle, C., Ritson, D. J., Duffy, C. D., & Sutherland, J. D. 2015, NatCh, 7, 301
Pegues, J., Öberg, K. I., Bergner, J. B., et al. 2020, ApJ, 890, 142
Pérez, S., Casassus, S., Hales, A., et al. 2020, ApJL, 889, L24
Pickett, H. M., Poynter, R. L., Cohen, E. A., et al. 1998, JQSRT, 60, 883

Pinte, C., Ménard, F., Duchêne, G., et al. 2018a, A&A, 609, A47
Pinte, C., Price, D. J., Ménard, F., et al. 2018b, ApJL, 860, L13
Pinte, C., Price, D. J., Ménard, F., et al. 2020, ApJL, 890, L9
Podio, L., Garufi, A., Codella, C., et al. 2020, A&A, 642, L7
Powner, M. W., Gerland, B., & Sutherland, J. D. 2009, Natur, 459, 239
Price-Whelan, A. M., Sipőcz, B. M., Günther, H. M., et al. 2018, AJ, 156, 123
Rab, C., Kamp, I., Dominik, C., et al. 2020, A&A, 642, A165
Rich, E. A., Wisniewski, J. P., Sitko, M. L., et al. 2020, ApJ, 902, 4
Rosenfeld, K. A., Andrews, S. M., Hughes, A. M., Wilner, D. J., & Qi, C. 2013, ApJ, 774, 16
Salinas, V. N., Hogerheijde, M. R., Mathews, G. S., et al. 2017, A&A, 606, A125
Salyk, C., Pontoppidan, K. M., Blake, G. A., Najita, J. R., & Carr, J. S. 2011, ApJ, 731, 130
Sastry, K. V. L. N., Helminger, P., Charo, A., Herbst, E., & De Lucia, F. C. 1981, ApJL, 251, L119
Shirley, Y. L. 2015, PASP, 127, 299
Sierra, A., Pérez, L. M., Zhang, K., et al. 2021, ApJS, 257, 14
Sokal, K. R., Deen, C. P., Mace, G. N., et al. 2018, ApJ, 853, 120
Teague, R. 2019, JOSS, 4, 1632
Teague, R., Bae, J., Bergin, E. A., Birnstiel, T., & Foreman-Mackey, D. 2018a, ApJL, 860, L12
Teague, R., Bae, J., Birnstiel, T., & Bergin, E. A. 2018b, ApJ, 868, 113
Teague, R., & Loomis, R. 2020, ApJ, 899, 157
Teague, R., Bae, J., Aikawa, Y., et al. 2021, ApJS, 257, 18
Terwisscha van Scheltinga, J., Hogerheijde, M. R., Cleeves, L. I., et al. 2021, ApJ, 906, 111
van der Walt, S., Colbert, S. C., & Varoquaux, G. 2011, CSE, 13, 22
van't Hoff, M. L. R., Harsono, D., Tobin, J. J., et al. 2020, ApJ, 901, 166
Virtanen, P., Gommers, R., Oliphant, T. E., et al. 2020, NatMe, 17, 261
Walsh, C., Loomis, R. A., Öberg, K. I., et al. 2016, ApJL, 823, L10
Watanabe, N., & Kouchi, A. 2002, ApJL, 571, L173
Watanabe, N., Nagaoka, A., Shiraki, T., & Kouchi, A. 2004, ApJ, 616, 638
Williams, J. P., & Cieza, L. A. 2011, ARA&A, 49, 67
Zhang, K., Booth, A. S., Law, C. J., et al. 2021, ApJS, 257, 5